

# TCMD: Transformational Complexity Based Distortion Metric for Perceptual Point Cloud Quality Assessment

Yujie Zhang, Qi Yang, Yifei Zhou, Xiaozhong Xu, Le Yang, Yiling Xu, *Member, IEEE*

**Abstract**—The goal of objective point cloud quality assessment (PCQA) research is to develop quantitative metrics that measure point cloud quality in a perceptually consistent manner. Merging the research of cognitive science and intuition of the human visual system (HVS), in this paper, we evaluate the point cloud quality by measuring the complexity of transforming the distorted point cloud back to its reference, which in practice can be approximated by the code length of one point cloud when the other is given. For this purpose, we first make space segmentation for the reference and distorted point clouds based on a 3D Voronoi diagram to obtain a series of local patch pairs. Next, inspired by the predictive coding theory, we utilize one space-aware vector autoregressive (SA-VAR) model to encode the geometry and color channels of each reference patch with and without the distorted patch, respectively. Assuming that the residual errors follow the multi-variate Gaussian distributions, the self-complexity of the reference and the transformational complexity between the reference and distorted samples are computed using covariance matrices. Additionally, the prediction terms generated by SA-VAR are introduced as one auxiliary feature to promote the final quality prediction. The effectiveness of the proposed transformational complexity based distortion metric (TCMD) is evaluated through extensive experiments conducted on five public point cloud quality assessment databases. The results demonstrate that the TCMD achieves state-of-the-art (SOTA) performance, and further analysis confirms its robustness across various scenarios.

**Index Terms**—Point Cloud Quality Assessment, Transformational Complexity, Predictive Coding, Vector Autoregressive Model

## 1 INTRODUCTION

Three-dimensional (3D) point cloud data has attracted much attention in recent years due to its wide applications, such as autopilot, virtual reality (VR), and 3D free-viewpoint broadcasting. In practical application scenarios, point cloud data is inevitably subject to a variety of distortions during acquisition, compression, transmission and rendering stages, which usually impair the perceptual quality of the human visual system (HVS) [1]. To establish the guidance of multiple point cloud applications targeted for human vision, point cloud quality assessment (PCQA) has been widely explored, which can further categorized into subjective PCQA and objective PCQA. Although subjective PCQA can provide accurate prediction, its application is limited due to the high cost in terms of time, money and rigorous testing environment. In comparison, objective PCQA intends to aims to design automatic approaches called PCQA metrics that can predict perceptual image quality consis-

*This paper is supported in part by National Natural Science Foundation of China (61971282, U20A20185). The corresponding author is Yiling Xu (e-mail: yl.xu@sjtu.edu.cn).*

*Y. Zhang, Y. Xu are from Cooperative Medianet Innovation Center, Shanghai Jiao Tong University, Shanghai, 200240, China, (e-mail: yujie19981026@sjtu.edu.cn, yl.xu@sjtu.edu.cn)*

*Q. Yang is with the with Tencent MediaLab, Shanghai, China, (email: chinoyang@tencent.com)*

*Y. Zhou is with the with Shanghai Maritime University, Shanghai, China, (email: 202110310163@stu.shmtu.edu.cn)*

*X. Xu is with the with Tencent MediaLab, Palo Alto, America, (email: xiaozhongxu@tencent.com)*

*L. Yang is with the Department of electrical and computer engineering, University of Canterbury, Christchurch 8041, New Zealand, (email: le.yang@canterbury.ac.nz)*

tently with human subjective evaluation, which is more convenient in practice due to lower cost and faster speed. PCQA metrics play a vital role in the quality of experience (QoE) oriented data processing. For instance, for point cloud compression or transmission, PCQA metrics can be used to derive constraints to achieve a better trade-off between the quality and compression rate or transmission bandwidth [2]. Moreover, PCQA metrics can also serve as loss functions to guide the model optimization in the learning-based point cloud enhancement tasks, such as spatial upsampling and completion [3]. Therefore, developing reliable and effective objective PCQA metrics correlated with human perception is highly desired. In this paper, we focus on full-reference (FR) PCQA metrics, which are designed for cases where the high-quality original point cloud is available as the reference for evaluating the quality of its distorted versions.

Early FR-PCQA metrics, e.g., point-to-point (p2po) and PSNR<sub>YUV</sub> [4], try to quantify point cloud distortions by calculating the geometry or color difference between each point of the distorted point cloud and its nearest point in the reference. However, these simple point-based metrics do not correlate well with human perception [5]. To solve this problem, some new PCQA metrics are proposed, and they can be generally categorized into 2D-based metrics [6], [7], [8], [9], [10], [11], [12], [13], and 3D-based metrics [5], [14], [15], [16], [17], [18], [19] according to whether the point cloud is projected into images. The 2D-based metrics first project the point cloud onto 2D planes at different viewing angles and then take advantage of the well-developed image processing tools to assist in PCQA. As for the 3D-based metrics, they try to predict point cloud quality by modeling

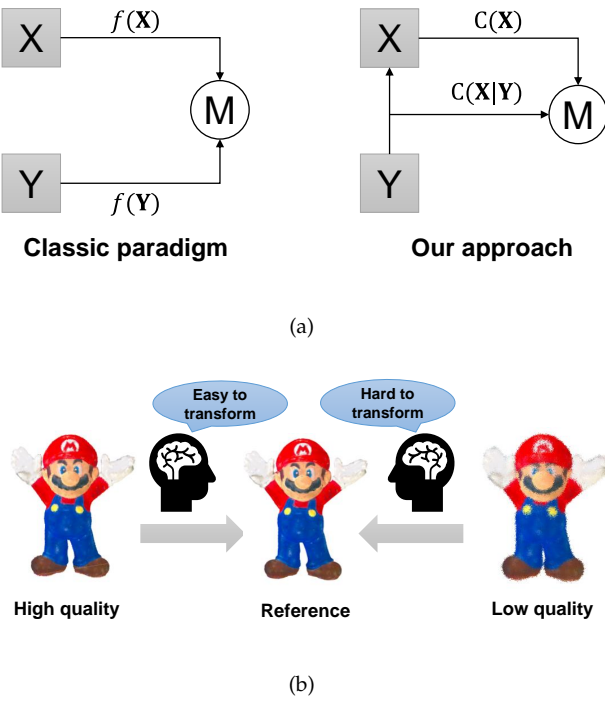


Fig. 1. We consider the FR-PCQA task from the perspective of transformational complexity. The more effort transforming the distorted point cloud to its reference need, the lower the quality of the distorted sample. (a) The paradigms of previous FR-PCQA works and our approach; (b) illustration of the motivation considered in this paper.

the 3D properties. Due to the irregular structure of point cloud data, the 3D-based metrics normally need to construct efficient data structures (e.g., surface [15], graph [5], mesh [20]) [21] to facilitate subsequent processing.

In general, the paradigm of most existing PCQA metrics, whether they are 2D-based or 3D-based, is to derive the quality score by comparing some perceptually sensitive features (e.g., gradient, curvature) extracted *separately* from the reference and the distorted point clouds. As shown in the left side of Fig. 1 (a), given two point clouds  $X$  and  $Y$ , the above paradigm can formulate their difference  $d(X, Y)$  as  $d(X, Y) = M(f(X), f(Y))$ , where  $f(\cdot)$  denotes the feature extraction operator and  $M(\cdot)$  denotes the pooling operator. The success of such methods is highly dependent on the effectiveness of the extracted features that rely on  $f(\cdot)$ . However, due to the irregular 3D structure of point cloud and rich distortion types, a single feature is usually insufficient for handling various types of distortions. To improve the robustness and accuracy of the metric, there is a tendency to use as many features as possible (e.g., PCQM [15] contains 8 features and PointPCA [19] contains 32 features), which can cause the metrics to become more and more bloated.

### 1.1 Motivation

In this paper, we propose to solve the problem of PCQA from a new perspective, namely, transformational complexity. In cognitive science, recent researches indicate that the similarity between two entities can be quantified using the "complexity" required to transform the representation of one

into that of the other [22], [23], which is called "*transformational complexity*" in this paper. According to prior empirical research, the more difficult the transformation from one entity to the other is, the less similar they would be. For instance, Hahn et al. [22] found, in three experiments, that the transformational complexity accurately predicts similarity ratings between simple graphics. As for those more complicated scenarios such as image processing, many similarity metrics based on the transformational complexity also shows competitive performance in several applications, including image retrieval [24], classification [25], etc.

Inspired by the success of transformational complexity in the above scenarios, in this paper, we intend to investigate its utility in PCQA. Intuitively, we suppose that the quality of one distorted point cloud can be quantified as the complexity or the amount of effort of transforming it into its corresponding reference. As shown in Fig. 1 (b), denoising one low quality sample disturbed by severe geometry Gaussian noise (GGN) is obviously more difficult than denoising one high quality sample disturbed by slight noise because severe geometry noise damages the structure of some regions (e.g., eyes), which brings higher complexity for recovery. More detailed visual samples can be found in Fig. 5. According to Fig. 5, given one reference point cloud patch, we intend to reconstruct it from multiple distorted patches impaired by GGN under three levels. As the level of distortion increases, it becomes evident that the reconstructed results (referred to as cross-prediction terms) of the distorted patches exhibit a greater disparity from the reference patch. We regard that the worse reconstruction results (i.e., with larger residuals) indicate larger transformational complexity, which further represents lower visual quality. To reduce the influence of intrinsic characteristics of different samples, *self-complexity* of the reference can be introduced as a normalization factor. Therefore, our method can be formulated as  $d'(X, Y) = M(C(X), C(X|Y))$  shown in the right side of Fig. 1 (a), where  $C(\cdot)$  and  $C(\cdot|Y)$  are the self-complexity of  $X$  and the transformational complexity between  $X$  and  $Y$ . Compared with the classic FR-PCQA paradigm, our approach avoids the complicated process of feature selection (i.e., finding  $f(\cdot)$ ) and instead addresses the quality evaluation as inferring the difficulty of recovering the reference from its distorted version.

One critical problem in our work is how to calculate the transformational complexity between two point clouds. The foundation of transformational complexity can call upon a particular branch of mathematics known as Kolmogorov complexity theory [26]. However, Kolmogorov complexity is in general an intractable quantity [27]. In practice, it is often approximated by the code length of the compressed data [28]. Intuitively, the more a given data can be compressed, the lower its complexity would be. Therefore, the transformational complexity between two entities is usually described as the code length of one entity when the other is given. For instance, Guha et al. [24] approximated the sparsity of an image by using the overcomplete dictionary extracted from the other image, where the sparse coefficients are used as a measure of transformational complexity. One important advantage of these compression-based approaches is their correlation with cognitive mechanisms. Recent developments in brain theory and neuroscience [29],

[30] show that human perception of external stimulus can be modeled as a process of predictive coding, which can be accounted for by the principles of parsimony and redundancy reduction. Therefore, deriving the transformational complexity via compression-based approaches possesses a tight connection to human perception. In our metric, we utilize the predictive coding theory to compute the transformational complexity.

## 1.2 Approach

We propose a novel FR-PCQA metric named transformational complexity based distortion metric (TCDM). Our metric is employed by the following three steps:

First, noting that local processing is more effective for quality assessment, we segment the reference and distorted point clouds into multiple local patch pairs based on one 3D Voronoi diagram (VD), which can ensure non-overlapping divisions and avoid the omission of points.

Secondly, we utilize one space-aware vector autoregressive (SA-VAR) model to encode the XYZ and RGB channels of each reference patch in cases with and without the corresponding distorted patch. Specifically, for each point in one reference patch, we use its neighbors in the reference and those in the distorted patch to predict itself using one autoregressive (AR) model, respectively.

Last, two complexity terms, i.e., self-complexity of the reference and transformational complexity between the reference and distorted samples, are calculated to derive a complexity-based similarity metric. The prediction terms generated by SA-VAR are introduced as one auxiliary feature to reach the final quality index.

Experimental results on five publicly available PCQA databases confirm that the proposed metric achieve state-of-the-art (SOTA) performance.

## 1.3 Contributions

The main contributions of the paper are summarized as:

- We propose a new point cloud quality metric called TCDM. Compared with existing PCQA metrics, our metric formulates the problem of quality evaluation from the perspective of measuring the transformational complexity, which is more effective than the methods that rely on separately extracted features.

- To compute the transformational complexity, we propose a SA-VAR model to encode both the geometry and color information of point cloud data. We introduce a predefined spatial weight to strengthen the awareness for irregular structure, and we utilize a multi-variate vector to capture the correlation between multiple channels.

- Our metric shows reliable performance in five publicly accessible databases. Further analyses reveal the model's generalization capability under various parameter setting.

The remainder of this paper proceeds as follows. Section 2 presents the related work. Section 3 formulates the FR-PCQA problem and the core idea of our metric. Implementation details of the proposed method are presented in Section 4. Section 5 give the experiment results. Conclusion are drawn in Section 6.

## 2 RELATED WORK

A handful of metrics have been proposed for FR-PCQA, which can be roughly categorized as 2D-based metrics and 3D-based metrics. Note that we classify early point-wise metrics (e.g., p2po and PSNR<sub>YUV</sub>) into 3D-based metrics because they do not have a point cloud projection operation. We give a brief review of these metrics in the following.

**2D-based metrics:** 2D-based metrics rely on quantifying point cloud distortion using projected images. To mimic the multi-view characteristic when observing 3D objects, researchers usually project the point cloud onto 2D planes at different viewing angles. In [7], Queiroz et al. projected the reference and distorted point clouds onto the six faces of a bounding box enclosing the point clouds and then concatenated the corresponding projected images. 2D PSNR was used to measure the distortions between the corresponding distorted and reference projected images. In [8], Alexiou et. al. conducted a study on the camera layouts around the point cloud, exploiting the impact of the number of projected images in 2D-based metrics. Different IQA methods (e.g., PSNR, SSIM [31] and VIFP [32]) were utilized to predict the quality of projected images and results showed that a larger number of projected views does not necessarily lead to better predictions of point cloud quality. To eliminate the misalignment between the reference and distorted projected images, Javaheri et al. [9] proposed to assign the same geometry to both the reference and distorted point clouds before the projection operation. Recently, to distinguish the background region and point cloud region in the projected images, Liu et al. [10] proposed one new metric based on the principle of information content weighted structural similarity (IW-SSIM) [33].

Except for the most commonly used color texture projected images, some geometry-related maps, such as depth and curvature maps, are also introduced into some 2D-based metrics to achieve more robust quality prediction. In [11], Yang et al. chose to project the 3D point cloud onto six perpendicular image planes of a cube to obtain both color texture and depth maps. Curvature maps were employed in [12] to serve as an auxiliary term. By introducing extra information to assist in quality assessment, the above metrics usually provided better performance than traditional IQA metrics that only utilized color texture projected images.

**3D-based metrics:** 3D-based metrics predict point cloud quality by modeling its 3D properties. Point-wise metrics were first applied to evaluate point cloud distortions, including p2po, point-to-plane (p2pl) and PSNR<sub>YUV</sub> [4]. Specifically, p2po and PSNR<sub>YUV</sub> calculated the distance between geometric coordinate or YUV values of each point pair. In comparison, p2pl computed the geometric distance between two points along the normal direction of the point cloud surface, which resulted in smaller errors for points closer to the surface. Researchers proposed some improvements for the above metrics in recent years. For instance, in [34], Alexious proposed a new metric named plane-to-plane (pl2pl), which utilized the normal vector of two points to derive the angular similarity. To alleviate the influence of outlier points, Javaheri et al. [35] proposed to use the Hausdorff distance for a specific percentage of data rather than the whole data set.

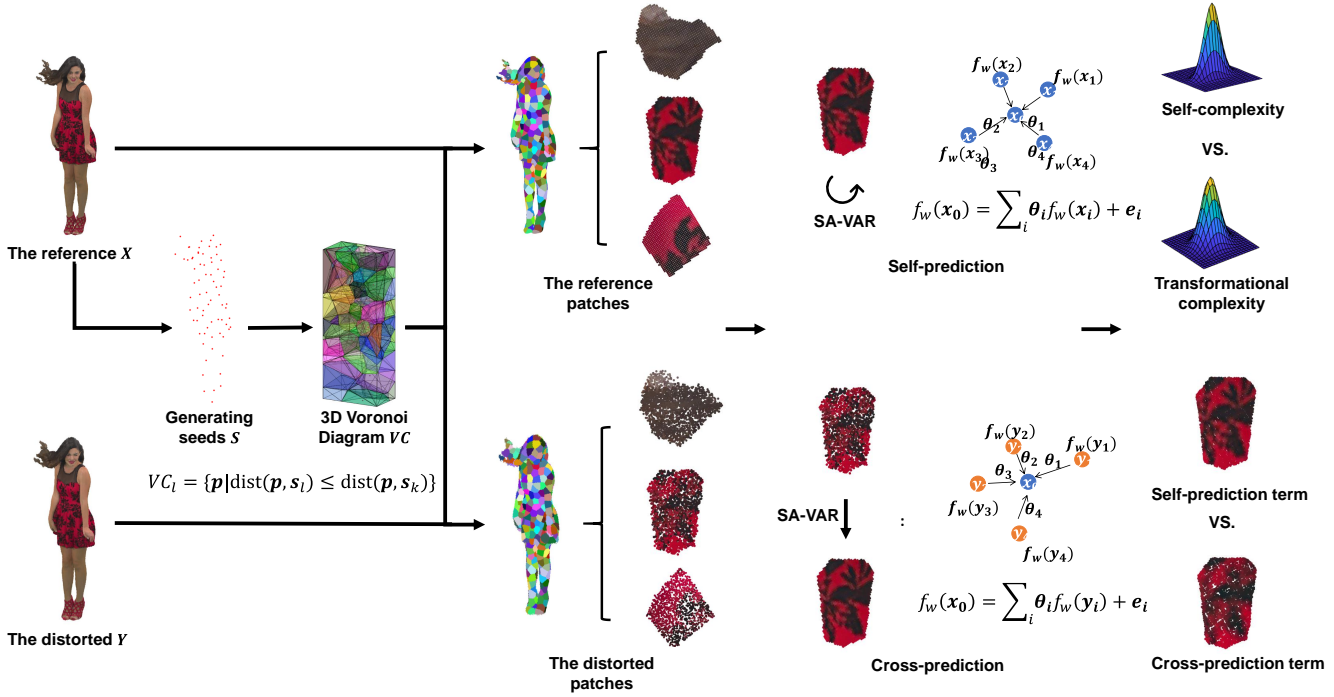


Fig. 2. The framework of the proposed TCDM. A point set is first sampled from the reference to serve as generating seeds of 3D Voronoi diagram. Utilizing the Voronoi diagram, both the reference and the distorted sample (impaired by geometry Gaussian noise) can be segmented into a series of local patch pairs. For each local patch pair, one space-aware vector autoregressive model is used to make the self-prediction for the reference patch and the cross-prediction between the patch pair. Two complexity terms and the prediction terms generated by SA-VAR is leveraged to derive the local quality index. All local quality indices are then fused to get the final quality score.

Point-wise metrics are not well correlated with subjective assessments, leading to unreliable prediction performance. Thus, some researchers proposed metrics that involve structural features to better predict subjective perception. Meynet et al. proposed PC-MSDM [14] based on local curvature similarity. Utilizing PC-MSDM, Meynet et al. extended it to PCQM [15], which utilized three curvature-related features and five color-related features to improve the prediction robustness. By constructing local graphs based on geometry information and regarding color values as graph signals, Yang et al. [5] developed GraphSIM to model the overall perception of HVS. A multi-scale version of GraphSIM was proposed by Zhang et al. in [16], which further took into account the multi-scale characteristics of human perception. In [18], Diniz et al. adapted the Local Binary Pattern (LBP) to point clouds. A variant descriptor called local luminance patterns (LLP) was proposed in [17], introducing a voxelization stage. PointPCA [19] proposed the use of geometric descriptors based on principal component analysis (PCA) to estimate structural distortions in point cloud contents.

As suggested in Section 1, most of the above metrics focus on how to extract more effective features. In other words, they intend to separately map the reference and its distorted version into two representations located in the same cognitive space that correlates well with human perception, and then represent quality in terms of the distance between the above two representations. In comparison, in this paper, we approach the FR-PCQA problem from a new perspective, i.e., evaluating the transformational complexity of getting the reference from its distorted version.

### 3 PROBLEM FORMULATION

In this section, we illustrate some basic concepts. We first present the formulation of FR-PCQA problem, then we detail the concept of transformational complexity and predictive coding theory and employ them in the FR-PCQA problem.

#### 3.1 Distortion Quantification of 3D Point Clouds

**Point Cloud Representation.** Let  $\mathbf{X}$  be a 3D point cloud with  $N$  points:  $\mathbf{X} = \{\mathbf{x}_1, \dots, \mathbf{x}_N\} \in \mathbb{R}^{N \times 6}$ , where each  $\mathbf{x}_i \in \mathbb{R}^6$  is a vector with 3D coordinates and three-channel color attributes, therefore,  $\mathbf{x}_i = [x, y, z, R, G, B] \equiv [\mathbf{x}_i^O, \mathbf{x}_i^I]$ , where  $\mathbf{x}_i^O = [x, y, z]$  and  $\mathbf{x}_i^I = [R, G, B]$ . The superscript "O" stands for geometric occupancy, and "I" stands for color intensity.

**Full-Reference Point Cloud Quality Assessment.** Given one reference point cloud  $\mathbf{X}$  and its distorted version  $\mathbf{Y}$ , an objective distortion quantification aims to measure the difference between the two samples. Considering that point clouds used for human perception tasks target for visualization, FR-PCQA intends to evaluate the visual quality of the distorted  $\mathbf{Y}$  with respect to its reference  $\mathbf{X}$ . Mathematically, the purpose of FR-PCQA is to find a model  $d(\cdot)$  that satisfies

$$\phi(d(\mathbf{X}, \mathbf{Y})) = s, \quad (1)$$

where  $s$  denotes the ground truth data called mean opinion score (MOS) acquired from subjective experiments;  $\phi(\cdot)$  denotes the nonlinear mapping to be learned, such as logistic regression or cubic regression.

As mentioned in Sections 1 and 2, most existing FR-PCQA metrics try to separately extract perceptually effective features from the reference and distorted point cloud. Therefore, we have

$$d(\mathbf{X}, \mathbf{Y}) = M(f(\mathbf{X}), f(\mathbf{Y})). \quad (2)$$

In practice,  $f(\cdot)$  intends to extract those visually sensitive features, such as gradient and curvature, and  $M(\cdot)$  can be the Minkowski pooling or similarity pooling [31].

### 3.2 Transformational Complexity

The complexity of an object is related to its randomness or redundancy. For example, the binary string 110101 is considered more complex than the string 010101, because the latter consists of repeating patterns and therefore is less random. The Kolmogorov complexity formalizes this concept. Specifically, given a finite signal  $\mathbf{x}$ , its Kolmogorov complexity  $K(\mathbf{x})$  is defined as the length of the shortest program complexity that can effectively produce on a universal computer, such as a Turing machine [36]. Based on the above definition, given two signals  $\mathbf{x}$  and  $\mathbf{y}$ , the transformational complexity between them is developed using the conditional Kolmogorov complexity  $K(\mathbf{x}|\mathbf{y})$ , which is defined as the length of the shortest program on a universal computer program to generate  $\mathbf{x}$  when  $\mathbf{y}$  is known.

Due to the non-computable nature of the Kolmogorov complexity [27], compression-based methods usually serve as an alternative to compute the transformational complexity. One pioneering work is the Normalized Compression Distance (NCD) [28], which considers the transformational complexity  $C(\mathbf{x}|\mathbf{y})$  as the code length of  $\mathbf{x}$  when  $\mathbf{y}$  is given. Specifically, the NCD can be formulated as

$$NCD(\mathbf{x}, \mathbf{y}) = \frac{\max \{C(\mathbf{x}|\mathbf{y}), C(\mathbf{y}|\mathbf{x})\}}{\max \{C(\mathbf{x}), C(\mathbf{y})\}},$$

where  $C(\cdot)$  is a compressor and the denominator  $\max \{C(\mathbf{x}), C(\mathbf{y})\}$  serves as a normalized factor.  $C(\mathbf{x}|\mathbf{y})$  is defined as the compressed length of  $\mathbf{x}$  when  $\mathbf{y}$  is given.

The NCD metric is regarded as an effective *similarity metric* and shows reliable performance in multiple applications such as clustering languages and music [37]. Inspired by its success in one-dimension (1D) data, various compression-based methods have been proposed for higher dimensional data types such as image and video [24], [38]. The key idea of these methods is how to encode the redundancy inherent in the data. In addition to the transformational complexity  $C(\mathbf{x}|\mathbf{y})$ , the self-complexity of  $\mathbf{x}$ , i.e.,  $C(\mathbf{x})$ , is usually utilized as a normalization factor. In general, we can formulate these compression-based similarity measures as follows,

$$d'(\mathbf{x}, \mathbf{y}) = M(C(\mathbf{x}), C(\mathbf{x}|\mathbf{y})), \quad (3)$$

where  $d'(\mathbf{x}, \mathbf{y})$  denotes the distance or similarity between two entities  $\mathbf{x}$  and  $\mathbf{y}$  ..

Although transformational complexity has achieved great success for 1D and 2D signals, there is no similar research related to 3D data. When we focus our attention on PCQA task, the connection between the compression-based methods and visual perception is also desirable to be constructed. To solve the above problems, our work tries to

apply the transformational complexity for PCQA task based on the predictive coding theory.

### 3.3 Predictive Coding Theory

Predictive coding is a leading theory on how the brain performs probabilistic inference [29]. It postulates that the human brain learns the statistical regularities inherent in the natural world, and reduces the redundancy by only encoding what is not predictable (the residual errors in prediction) [39]. The underlying assumption of this theory is that our cognitive process is governed by an internal generative model in the brain. With this internal model, the brain can generate the corresponding predictions for the encountered visual scenes. Mathematically, given a brain internal model for visual perception, denoted as  $G$ , it can adjust its parameter  $\Theta$  to minimize the negative log-likelihood function  $-\log p(\mathbf{x}|\Theta, G)$ , which is usually described as “code length” of  $\mathbf{x}$  [39] due to the same formulation as Shannon’s entropy. For some predictive coding algorithms such as traditional linear predictive coding [40], [41], the optimal parameter  $\Theta$  can be solved by

$$\hat{\Theta} = \arg \min_{\Theta} -\log p(\mathbf{x}|\Theta, G). \quad (4)$$

In general, predictive coding theory shares similar principles of redundancy reduction with information compression, inspiring a large number of compression algorithms [42], [43]. Therefore, we can model our visual perception as one compression process and relate the minimized negative log-likelihood function to the concept of complexity. To achieve the goal of PCQA, we need one efficient quality-related internal model  $G$ . In our work, one space-aware vector autoregressive model is employed as  $G$ , which is described meticulously in Section 4. Then, given two point clouds  $\mathbf{X}$  and  $\mathbf{Y}$ , we can derive the self-complexity of  $\mathbf{X}$ ,  $C(\mathbf{X})$ , via one self-prediction process, and the transformational complexity between two point clouds,  $C(\mathbf{X}|\mathbf{Y})$ , via one cross-prediction process as follows,

$$\begin{aligned} C(\mathbf{X}) &= \min_{\Theta_s} -\log p(\mathbf{X}|\Theta_s, G), \\ C(\mathbf{X}|\mathbf{Y}) &= \min_{\Theta_t} -\log p(\mathbf{X}|\mathbf{Y}, \Theta_t, G), \end{aligned} \quad (5)$$

where  $\Theta_s$  and  $\Theta_t$  denote the model parameters in the self-prediction and cross-prediction processes. We can derive one complexity-based similarity metric according to Eq. (3), i.e.,  $d'(\mathbf{X}, \mathbf{Y}) = M(C(\mathbf{X}), C(\mathbf{X}|\mathbf{Y}))$ , which can serve as one quality feature for PCQA.

## 4 PROPOSED METHOD

In this part, we first introduce the overall framework of the proposed model in Section 4.1. Then, we give the detailed implementation for each module.

### 4.1 Architecture

We show the overall framework of our model in Fig. 2. Taking the reference  $\mathbf{X}$  and the distorted point cloud  $\mathbf{Y}$  as the input, we first extract a series of points from  $\mathbf{X}$  via farthest point sampling (FPS). Utilizing the sampling points as the generating seeds, we make space segmentation to derive a 3D Voronoi diagram (VD), which is consist of

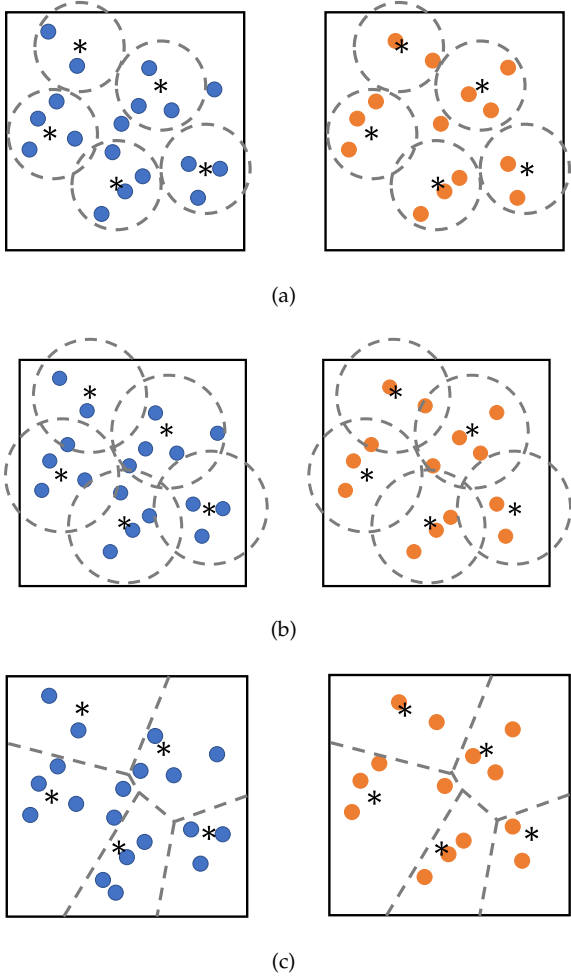


Fig. 3. The comparison of several segmentation strategies for PCQA task. Note that the “\*” denotes the spherical center in (a) and (b), and the generating seeds in (c). Both (a) and (b) use a series of spherical spaces to bound points in the reference and the distorted point clouds. However, too small spherical radius in (a) is not enough to cover all points in the reference while too large spherical radius in (b) results in unnecessary overlaps. In comparison, (c) utilizes the Voronoi Diagram for space segmentation, which achieves non-overlapping divisions and avoids the omission of points.

many Voronoi cells (VCs). Each cell in the VD bounds one local patch pair in the  $\mathbf{X}$  and  $\mathbf{Y}$ . Next, for each local patch pair, one SA-VAR is used to make self-prediction and cross-prediction for the reference patch, which results in two complexity terms, i.e., the self-complexity of the reference patch and the transformational complexity between the local patch pair. The prediction terms generated by SA-VAR serve as complementary terms to help generate the local quality index. We finally fuse all local quality indices to get the final quality score.

#### 4.2 Space Segmentation via Voronoi Diagram

For PCQA, it is preferred to process the point cloud locally rather than globally. First, dense point clouds have millions of disordered points distributed in 3D space, which leads to high computational cost when taking the entire point cloud as input. Especially, when the complexity of one algorithm reaches  $O(N^2)$  or higher, the practical computational cost

of global processing will be prohibitive. Secondly, due to the multi-view characteristic when observing 3D objects and the foveation mechanisms [44] of HVS, the human observer often only perceives a localized area of the point cloud at one time. Finally, visual masking effects differentiate the perceptual quality degradation caused by the same level of distortion in different regions [45].

For the FR-PCQA task, two critical steps need to be determined for local processing, that is, how to divide the point cloud into local patches and how to construct the patch correspondence between the reference and the distorted point clouds. The existing methods usually try to bound points in the reference and its distorted version by a series of spherical spaces [5], [16]. However, the number of divisions and the size of the spherical radius in the method are often difficult to determine. As illustrated in Fig. 3 (a) and (b), given a fixed number of divisions, too small radius is not enough to cover the entire point cloud while too large radius results in many overlaps and involves unnecessary computational cost. Some researchers [45] leverage  $K$ -means clustering for the reference and then determine the corresponding clusters of the distorted version by nearest-neighbor searching, which may cause some points in the distorted point cloud to be ignored. To avoid the above problems, our work uses a 3D Voronoi diagram (VD) to realize space segmentation for point clouds, which can achieve non-overlapping divisions and avoid the omission of points during the process of correspondence construction.

The 3D VD divides the 3D space into many *non-overlapping* convex polyhedrons called Voronoi cells (VCs) such that each polyhedron contains exactly one generating seed, and every point in a given cell is much closer to the corresponding generating seed than to any other generating seeds. Let  $\mathbf{p} \in \mathbb{R}^3$  be a point in the Euclidean space. Assuming a set of points as the generating seeds  $\mathbf{S} = \{\mathbf{s}_l \in \mathbb{R}^3\}_{l=1}^L$ , the VD generated by  $\mathbf{S}$  is defined by the nearest-neighbor principle, i.e., the cell  $VC_l$  corresponding the seed  $\mathbf{s}_l$  is defined by

$$VC_l = \{\mathbf{p} \in \mathbb{R}^3 \mid \text{dist}(\mathbf{p}, \mathbf{s}_l) \leq \text{dist}(\mathbf{p}, \mathbf{s}_k), \text{if } k \neq l\}, \quad (6)$$

where  $\text{dist}(\cdot)$  denotes the Euclidean distance between two points. Clearly, one cell  $VC_l$  represents one convex polyhedron space centered around the seeds  $\mathbf{s}_l$  bounded by a series of planes, which is locally finite and has a non-empty interior. All VCs cover the whole 3D space without overlap and omission. Therefore, we can bound points in both reference and distorted point clouds via these cells.

Specifically, let  $\mathbf{X} = \{\mathbf{x}_i \in \mathbb{R}^6\}_{i=1}^N$  and  $\mathbf{Y} = \{\mathbf{y}_j \in \mathbb{R}^6\}_{j=1}^M$  be the reference and the distorted point clouds with  $N$  and  $M$  points, respectively. We first derive the generating seed set  $\mathbf{S}$  from  $\mathbf{X}$  via the farthest point sampling (FPS) [46], i.e.,

$$\mathbf{S} = [\Upsilon(\mathbf{X})]_L \in \mathbb{R}^{L \times 6}, L \ll N,$$

where  $\Upsilon(\cdot)$  represents the FPS operation. The number of seeds is empirically set to be  $L = 400$  in our work.

Next, for each seed  $\mathbf{s}_l$ , we derive its corresponding cell  $VC_l$  according to Eq. (6). Then we can respectively obtain the local patch pair bounded in  $\mathbf{X}$  and  $\mathbf{Y}$  by the  $VC_l$  as

$$\begin{aligned} \mathbf{X}_l &= \{\mathbf{x}_i | \mathbf{x}_i^O \in VC_l\} \in \mathbb{R}^{N_l \times 6}, \\ \mathbf{Y}_l &= \{\mathbf{y}_j | \mathbf{y}_j^O \in VC_l\} \in \mathbb{R}^{M_l \times 6}, \end{aligned} \quad (7)$$

where  $N_l$  and  $M_l$  denote the point number of two local patches. We have  $\mathbf{P}_X = \{\mathbf{X}_l\}_{l=1}^L$  and  $\mathbf{P}_Y = \{\mathbf{Y}_l\}_{l=1}^L$  for all local patches. Note that all patches in  $\mathbf{P}_X$  or  $\mathbf{P}_Y$  are non-overlapping and no point is omitted during the above process.

Finally, considering relative coordinates are more meaningful than absolute coordinates when human eyes focus on one local region, we align patches via translation so that each patch has its generating seed at the origin, i.e.,

$$\begin{aligned}\tilde{\mathbf{X}}_l &= \{\tilde{\mathbf{x}}_i\}_{i=1}^{N_l} = [\mathbf{X}_l^O - \mathbf{S}_{N_l}, \mathbf{X}_l^I] \in \mathbb{R}^{N_l \times 6}, \\ \tilde{\mathbf{Y}}_l &= \{\tilde{\mathbf{y}}_j\}_{j=1}^{M_l} = [\mathbf{Y}_l^O - \mathbf{S}_{M_l}, \mathbf{Y}_l^I] \in \mathbb{R}^{M_l \times 6},\end{aligned}\quad (8)$$

where  $\tilde{\mathbf{x}}_i = [\tilde{\mathbf{x}}_i^O, \tilde{\mathbf{x}}_i^I] = [\mathbf{x}_i^O - \mathbf{s}_l^O, \mathbf{x}_i^I]$  denotes the translated point of  $\mathbf{x}_i$  and  $\mathbf{S}_{N_l} = [(\mathbf{s}_l^O)_{\times N_l}] \in \mathbb{R}^{N_l \times 3}$  denotes the seed coordinate matrix of  $\mathbf{s}_l$ .  $\tilde{\mathbf{y}}$  and  $\mathbf{S}_{M_l}$  have a similar meaning as above. The translated local patch pair, i.e.,  $\tilde{\mathbf{X}}_l$  and  $\tilde{\mathbf{Y}}_l$ , are used for subsequent local processing.

### 4.3 Deriving Complexity Based on SA-VAR

As mentioned in Section 3.2, predictive coding theory shares a similar principle of redundancy reduction with information compression and possesses a good connection to human visual perception, which makes it an effective theorem basis to measure the complexity of the data. In general, our basic idea is to relate the complexity to the negative log-likelihood function after minimization.

One obvious fact is that any quantitative application of Eq. (4) needs to assume the brain generative model  $G$  first. A model with higher expressive power might approximate the brain better, but incurs higher computational complexity. In some previous works [47], [48], [49], [50], [51], the autoregressive (AR) model is widely used due to its good local adaptability and low computational cost. The classic paradigm of the AR model used in the image domain can be written as

$$f_i = \sum_{j=1}^K \theta_j f_j + e_i = f(\mathcal{N}_i^K) \boldsymbol{\theta} + e_i, \quad (9)$$

where  $f_i$  represent the  $i$ -th pixel value in the given image;  $f(\mathcal{N}_i^K) \in \mathbb{R}^K$  is a vector consisting  $K$  nearest neighbors of the  $i$ -th pixel and  $e_i$  is the additive Gaussian residual noise with zero mean. The above AR model achieves satisfying performance in many image processing algorithms (e.g., interpolation [49], compression [50], quality assessment [47], etc.)

However, it is worth pointing out that the AR model shown in Eq. (9) only concentrates on a single channel (e.g., luminance channel in the image domain), which is effective enough for regular single-channel data such as gray images. In comparison, the colored point cloud studied in this paper is typical multi-channel data and there exists some correlation between different feature channels (e.g., XYZ and RGB channels) [52]. It is believed that our HVS can capture such correlation to realize the final quality decision. Therefore, in order to exploit the inter-channel and intra-channel correlation of point cloud data simultaneously, we propose to utilize one space-aware vector autoregressive model (SA-VAR) to encode multiple channels.

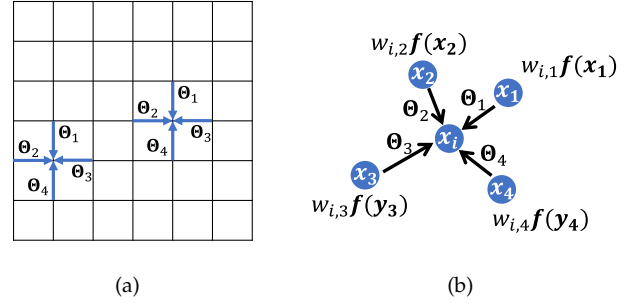


Fig. 4. Two-dimensional autoregressive model and our space-aware vector autoregressive model.

Specifically, given one translated local patch pair  $\tilde{\mathbf{X}}_l$  and  $\tilde{\mathbf{Y}}_l$ , we shall compute the self-complexity  $C(\tilde{\mathbf{X}}_l|\tilde{\mathbf{X}}_l)$  and the transformational complexity  $C(\tilde{\mathbf{X}}_l|\tilde{\mathbf{Y}}_l)$ . Here we denote the self-complexity by  $C(\tilde{\mathbf{X}}_l|\tilde{\mathbf{X}}_l)$  rather than  $C(\tilde{\mathbf{X}}_l)$  because the AR model can be regarded as one self-generation model when only applying for  $\tilde{\mathbf{X}}_l$  itself. We detail the calculation process in the following.

**Calculating Self-Complexity via Self-Prediction.** We first show the classic VAR model for encoding multiple variables in  $\tilde{\mathbf{X}}_l$ . For one point  $\tilde{\mathbf{x}}_i$  in  $\tilde{\mathbf{X}}_l$ , the VAR leverages the neighbors of  $\tilde{\mathbf{x}}_i$  in  $\tilde{\mathbf{X}}_l$  to make self-prediction for its feature, i.e.,

$$f(\tilde{\mathbf{x}}_i) = \sum_{\tilde{\mathbf{x}}_j \in \mathcal{N}_{\tilde{\mathbf{x}}_i, K}} \Theta_j f(\tilde{\mathbf{x}}_j) + \mathbf{e}_i = \Theta_s f(\mathcal{N}_{\tilde{\mathbf{x}}_i, K}^{\tilde{\mathbf{X}}_l}) + \mathbf{e}_i, \quad (10)$$

where  $f(\tilde{\mathbf{x}}_i) \in \mathbb{R}^d$  represents one  $d$ -dimension feature of  $\tilde{\mathbf{x}}_i$ , accounting for  $\tilde{\mathbf{x}}_i^O$  or  $\tilde{\mathbf{x}}_i^I$  in our work. In other words, we utilize the VAR to encode XYZ and RGB channels individually.  $\mathcal{N}_{\tilde{\mathbf{x}}_i, K}^{\tilde{\mathbf{X}}_l} \subset \tilde{\mathbf{X}}_l$  denotes  $\tilde{\mathbf{x}}_i$ 's  $K$  closest points in  $\tilde{\mathbf{X}}_l$  (Note that the closest point, i.e.,  $\tilde{\mathbf{x}}_i$  itself, is excluded) and  $f(\mathcal{N}_{\tilde{\mathbf{x}}_i, K}^{\tilde{\mathbf{X}}_l}) = [f(\tilde{\mathbf{x}}_1); f(\tilde{\mathbf{x}}_2); \dots; f(\tilde{\mathbf{x}}_l)] \in \mathbb{R}^{Kd}$  denotes the feature matrix of the neighbors.  $\Theta_j \in \mathbb{R}^{d \times d}$  and  $\Theta_s = [\Theta_1; \Theta_2; \dots; \Theta_K] \in \mathbb{R}^{d \times Kd}$  denotes the parameter set of VAR.  $\mathbf{e}_j \sim \mathcal{N}(0, \Sigma_s)$  is assumed to belong to multivariate Gaussian distribution, where  $\Sigma_s \in \mathbb{R}^{d \times d}$ .

As shown in Fig. 4 (a), the existing assumption of the traditional 2D AR is that all points/pixels locate in a regular grid shape [53], in which case the parameter  $\Theta_s$  shares the same spatial structure in different locations. In comparison, the topological condition of the point cloud is irregular as shown in Fig. 4 (b). To adapt the VAR to point cloud data, we add a spatial weight for each neighbor in Eq. (10) to produce one space-aware VAR model, i.e.,

$$\begin{aligned}f(\tilde{\mathbf{x}}_i) &= \sum_{\tilde{\mathbf{x}}_j \in \mathcal{N}_{\tilde{\mathbf{x}}_i, K}} w_{i,j} \Theta_j f(\tilde{\mathbf{x}}_j) + \mathbf{e}_i \\ &= \Theta_s f_w(\mathcal{N}_{\tilde{\mathbf{x}}_i, K}^{\tilde{\mathbf{X}}_l}) + \mathbf{e}_i, \\ w_{i,j} &= \frac{d_{i,j}}{\sum_j d_{i,j}}, d_{i,j} = \frac{1}{1 + e^{-\frac{\|\tilde{\mathbf{x}}_i^O - \tilde{\mathbf{x}}_j^O\|_2}{\eta}}},\end{aligned}\quad (11)$$

where  $\eta$  denotes the geometry variance within  $\mathcal{N}_{\tilde{\mathbf{x}}_i, K}^{\tilde{\mathbf{X}}_l}$ . The weight  $w_{i,j}$  is related to the spatial distance between  $\tilde{\mathbf{x}}_i$  and  $\tilde{\mathbf{x}}_j$ , which strengthens the AR's capability of capturing irregular spatial structure.

Now we apply the above SA-VAR for all points in the local patch  $\tilde{\mathbf{X}}_l = \{\tilde{\mathbf{x}}_i\}_{i=1}^{N_l}$  and have

$$f(\tilde{\mathbf{X}}_l) = \Theta_s f_w(\mathcal{N}_{\tilde{\mathbf{X}}_l, K}^{\tilde{\mathbf{X}}_l}) + \mathbf{E}, \quad (12)$$

where  $f(\tilde{\mathbf{X}}_l)$ ,  $\mathbf{E} \in \mathbb{R}^{d \times N_l}$  denote the feature and noise matrix of  $\tilde{\mathbf{X}}_l$ ;  $f_w(\mathcal{N}_{\tilde{\mathbf{X}}_l, K}^{\tilde{\mathbf{X}}_l}) \in \mathbb{R}^{kd \times N_l}$  denotes the weighted neighbor feature matrix of the whole patch  $\tilde{\mathbf{X}}_l$ . To facilitate the calculation, we vectorize the above representation as

$$f_v(\tilde{\mathbf{X}}_l) = (f_w^T(\mathcal{N}_{\tilde{\mathbf{X}}_l, K}^{\tilde{\mathbf{X}}_l}) \otimes \mathbf{I}_d) \Theta_{s,v} + \mathbf{E}_v, \quad (13)$$

where  $f_v(\tilde{\mathbf{X}}_l)$ ,  $\mathbf{E}_v \in \mathbb{R}^{N_l d}$  and  $\Theta_{s,v} \in \mathbb{R}^{K d^2}$  denote the vectorized representation of  $f(\tilde{\mathbf{X}}_l)$ ,  $\mathbf{E}$  and  $\Theta_s \otimes$  represents the Hadamard product;  $\mathbf{I}_d \in \mathbb{R}^{d \times d}$  is the  $d$ -dimension identity matrix. Considering  $\mathbf{E}_v \sim \mathcal{N}(0, \mathbf{I}_{N_l} \otimes \Sigma_s)$ , we have the likelihood

$$p(\tilde{\mathbf{X}}_l | \Theta_{s,v}, G) = \frac{1}{(2\pi)^{\frac{N_l d}{2}} |\mathbf{I}_{N_l} \otimes \Sigma_s|^{\frac{1}{2}}} e^{-\frac{1}{2} \mathbf{E}_v^T (\mathbf{I}_{N_l} \otimes \Sigma_s)^{-1} \mathbf{E}_v}. \quad (14)$$

The negative log-likelihood term can be further written as

$$\begin{aligned} -\log p(\tilde{\mathbf{X}}_l | \Theta_{s,v}, G) &= \frac{N_l d}{2} \log 2\pi + \frac{N_l}{2} \log |\Sigma_s| \\ &+ \frac{1}{2} \text{Tr}(\mathbf{E}_v^T \Sigma_s^{-1} \mathbf{E}_v). \end{aligned} \quad (15)$$

According to Eq. (4) and Eq. (15), we can derive the closed-form solution of  $\Theta_{s,v}$  and  $\Sigma_s$  as

$$\begin{aligned} \hat{\Theta}_{s,v} &= [f_w(\mathcal{N}_{\tilde{\mathbf{X}}_l, K}^{\tilde{\mathbf{X}}_l}) f_w^T(\mathcal{N}_{\tilde{\mathbf{X}}_l, K}^{\tilde{\mathbf{X}}_l})]^{-1} f_w(\mathcal{N}_{\tilde{\mathbf{X}}_l, K}^{\tilde{\mathbf{X}}_l}) \otimes \mathbf{I}_d] f_v(\tilde{\mathbf{X}}_l) \\ \hat{\Sigma}_s &= \frac{1}{N_l} [f(\tilde{\mathbf{X}}_l) - \hat{\Theta}_{s,v} f_w(\mathcal{N}_{\tilde{\mathbf{X}}_l, K}^{\tilde{\mathbf{X}}_l})] [f(\tilde{\mathbf{X}}_l) - \hat{\Theta}_{s,v} f_w(\mathcal{N}_{\tilde{\mathbf{X}}_l, K}^{\tilde{\mathbf{X}}_l})]^T \end{aligned} \quad (16)$$

where  $\hat{\Theta}_s$  denotes the reshaped matrix form of  $\hat{\Theta}_{s,v}$ .

Inducing the optimal estimation  $\hat{\Theta}_{s,v}$  and  $\hat{\Sigma}_s$  in Eq. (15), we obtain the minimized negative log-likelihood function as:

$$-\log p(\tilde{\mathbf{X}}_l | \hat{\Theta}_{s,v}, G) = \frac{N_l d}{2} (\log 2\pi + 1) + \frac{N_l}{2} \log |\hat{\Sigma}_s|. \quad (17)$$

Eq. (17) represents the differential entropy of the multivariate Gaussian distribution, which is only relevant to the determinant of the estimated covariance matrix when fixing  $N_l$  and  $d$ . Therefore, we represent the self-complexity of  $\tilde{\mathbf{X}}_l$  as,

$$C(\tilde{\mathbf{X}}_l | \tilde{\mathbf{X}}_l) = |\hat{\Sigma}_s|. \quad (18)$$

In practice, we respectively apply the SA-VAR for XYZ and RGB channels, in which cases we have  $f(\tilde{\mathbf{X}}_l) = (\tilde{\mathbf{X}}_l^O)^T$  and  $f(\tilde{\mathbf{X}}_l) = (\tilde{\mathbf{X}}_l^I)^T$ . We finally represent the self-complexity of geometry and color channels using  $C^O(\tilde{\mathbf{X}}_l | \tilde{\mathbf{X}}_l)$  and  $C^I(\tilde{\mathbf{X}}_l | \tilde{\mathbf{X}}_l)$ .

**Calculating Transformational Complexity via Cross-Prediction.** We further consider the transformational complexity between  $\tilde{\mathbf{X}}_l$  and  $\tilde{\mathbf{Y}}_l$ . As mentioned in Section 3.2, the transformation complexity  $C(\tilde{\mathbf{X}}_l | \tilde{\mathbf{Y}}_l)$  can be considered as the code length of  $\tilde{\mathbf{X}}_l$  when  $\tilde{\mathbf{Y}}_l$  is given. Therefore, we utilize the neighbors of  $\tilde{\mathbf{x}}_i$  in  $\tilde{\mathbf{Y}}_l$  to make one cross-prediction for  $\tilde{\mathbf{x}}_i$ , i.e.,

$$\begin{aligned} f(\tilde{\mathbf{X}}_l) &= \Theta_t f_w(\mathcal{N}_{\tilde{\mathbf{X}}_l, K}^{\tilde{\mathbf{Y}}_l}) + \mathbf{E}, \\ f_v(\tilde{\mathbf{X}}_l) &= (f_w^T(\mathcal{N}_{\tilde{\mathbf{X}}_l, K}^{\tilde{\mathbf{Y}}_l}) \otimes \mathbf{I}_d) \Theta_{t,v} + \mathbf{E}_v, \end{aligned} \quad (19)$$

where  $\mathcal{N}_{\tilde{\mathbf{X}}_l, K}^{\tilde{\mathbf{Y}}_l} \subset \tilde{\mathbf{Y}}_l$  has a similar meaning with  $\mathcal{N}_{\tilde{\mathbf{X}}_l, K}^{\tilde{\mathbf{X}}_l}$ .  $\mathbf{E}_v \sim \mathcal{N}(0, \mathbf{I}_{N_l} \otimes \Sigma_t)$ . The likelihood function can be written as

$$p(\tilde{\mathbf{X}}_l | \tilde{\mathbf{Y}}_l, \Theta_{t,v}, G) = \frac{1}{(2\pi)^{\frac{N_l}{2}} |\mathbf{I}_{N_l} \otimes \Sigma_t|^{\frac{1}{2}}} e^{-\frac{1}{2} \mathbf{E}_v^T (\mathbf{I}_{N_l} \otimes \Sigma_t)^{-1} \mathbf{E}_v} \quad (20)$$

According to Eq. (15)-(18), the minimized negative log term of Eq. (20) is only related to  $\hat{\Sigma}_t$ . Therefore, we represent the transformational complexity between  $\tilde{\mathbf{X}}_l$  and  $\tilde{\mathbf{Y}}_l$  as,

$$C(\tilde{\mathbf{X}}_l | \tilde{\mathbf{Y}}_l) = |\hat{\Sigma}_t| \quad (21)$$

where  $\hat{\Sigma}_t$  can be obtained via the same paradigm as Eq. (16). Similarly, we respectively derive  $C^O(\tilde{\mathbf{X}}_l | \tilde{\mathbf{Y}}_l)$  and  $C^I(\tilde{\mathbf{X}}_l | \tilde{\mathbf{Y}}_l)$ , which denotes the transformation complexity of geometry and color channels.

**Pooling Strategy.** As illustrated in Section 3.2, we need to choose a pooling strategy to merge the self-complexity and transformational complexity. Considering the success of similarity measurement in SSIM [31], we define two local complexity based features related to geometry and color channels as

$$\begin{aligned} F_{1,l}^O &= \frac{2C^O(\tilde{\mathbf{X}}_l | \tilde{\mathbf{X}}_l) \cdot C^O(\tilde{\mathbf{X}}_l | \tilde{\mathbf{Y}}_l) + T}{(C^O(\tilde{\mathbf{X}}_l | \tilde{\mathbf{X}}_l))^2 + (C^O(\tilde{\mathbf{X}}_l | \tilde{\mathbf{Y}}_l))^2 + T} \\ F_{1,l}^I &= \frac{2C^I(\tilde{\mathbf{X}}_l | \tilde{\mathbf{X}}_l) \cdot C^I(\tilde{\mathbf{X}}_l | \tilde{\mathbf{Y}}_l) + T}{(C^I(\tilde{\mathbf{X}}_l | \tilde{\mathbf{X}}_l))^2 + (C^I(\tilde{\mathbf{X}}_l | \tilde{\mathbf{Y}}_l))^2 + T}, \end{aligned} \quad (22)$$

where  $T$  is a small no-zero constant to prevent numerical instability.

#### 4.4 Auxiliary Feature Based on Prediction Terms

Except for complexity terms shown in Eq. (18) and (21), prediction terms in the prediction process are also meaningful. Specifically, we define

$$\begin{aligned} \hat{\mathbf{X}}_l &= \{\hat{\mathbf{x}}_i\}_{i=1}^{N_l} = [\hat{\Theta}_s f_w(\mathcal{N}_{\tilde{\mathbf{X}}_l, K}^{\tilde{\mathbf{X}}_l})]^T \in \mathbb{R}^{N_l \times 6}, \\ \hat{\mathbf{Y}}_l &= \{\hat{\mathbf{y}}_i\}_{i=1}^{N_l} = [\hat{\Theta}_t f_w(\mathcal{N}_{\tilde{\mathbf{X}}_l, K}^{\tilde{\mathbf{Y}}_l})]^T \in \mathbb{R}^{N_l \times 6}, \end{aligned} \quad (23)$$

which represent the reconstructed patches of applying SA-VAR for the self-prediction of  $\tilde{\mathbf{X}}_l$  and for the cross-prediction between  $\tilde{\mathbf{X}}_l$  and  $\tilde{\mathbf{Y}}_l$ . We show the cross-prediction terms of three different distortions under different levels in Fig. 5. Two reasons motivate us to utilize the above prediction terms: i) There exists a perfect *point-to-point correspondence* between  $\tilde{\mathbf{X}}_l$  and  $\tilde{\mathbf{Y}}_l$  because both  $\hat{\mathbf{x}}_i$  and  $\hat{\mathbf{y}}_i$  denote the predictions for  $\tilde{\mathbf{x}}_i$ , which is highly desired for point cloud processing. ii) According to the predictive coding theory, the prediction term can be regarded as the optimized perceptual representation in our brain [48], which also reflects visual quality to some extent. For instance, in Fig. 5, we can observe that the cross-prediction term of the patch with the highest geometry Gaussian noise (GGN) level does not restore the patch shape and color well, which can be explained by the fact that too disorderly points bring high difficulty for our brain to achieve perfect reconstruction. Meanwhile, the formulations of the complexity terms are related to the residual errors between the prediction and the ground truth. Therefore, it is believed that prediction

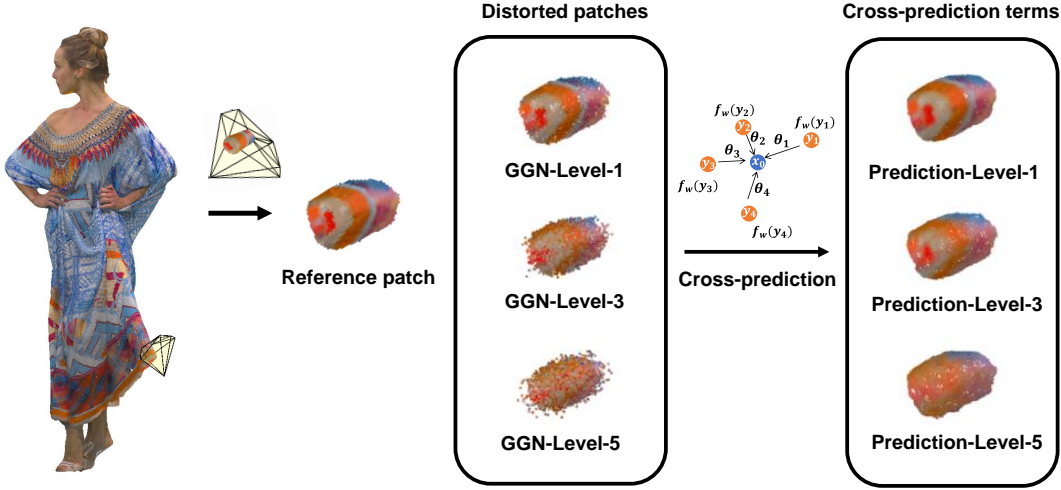


Fig. 5. Comparison of the cross-prediction terms of distorted patches impaired by geometry Gaussian noise (GGN) under different levels.

terms are complementary to the complexity terms for modeling the whole perception of point cloud distortions.

Consider the point index of  $\hat{\mathbf{X}}_l$  and  $\hat{\mathbf{Y}}_l$  is from 1 to  $N_l$ . To better exploit the point-to-point correspondence between  $\hat{\mathbf{X}}_l$  and  $\hat{\mathbf{Y}}_l$ , we first calculate one point-wise difference vector between  $\hat{\mathbf{x}}_i$  and its neighbors in  $\hat{\mathbf{X}}_l$  as follows,

$$\mathbf{v}_{\hat{\mathbf{x}}_i} = \{g(\hat{\mathbf{x}}_i, \hat{\mathbf{x}}_j)\}_{j \in Id_i} \in \mathbb{R}^K$$

$$g(\hat{\mathbf{x}}_i, \hat{\mathbf{x}}_j) = \left( \sum_d^3 k_d |(\hat{\mathbf{x}}_i^I)_j - (\hat{\mathbf{x}}_j^I)_j| + 1 \right) \cdot \|\hat{\mathbf{x}}_i^O - \hat{\mathbf{x}}_j^O\|_2, \quad (24)$$

where  $Id_i = \{j | \hat{\mathbf{x}}_j \in \mathcal{N}_{\hat{\mathbf{x}}_i, K}^{\hat{\mathbf{X}}_l}\}$  denotes the indices of  $\hat{\mathbf{x}}_i$ 's neighbors;  $k_d$  represents the weighting factors between different color channel, i.e.,  $k_R : k_G : k_B = 1 : 2 : 1$  [3].  $g(\cdot)$  can be regarded as one combination of geometry difference used in p2po and color difference used in PSNR<sub>YUV</sub>, which reflects both geometric and attribute discrepancies between one point pair.

Then we utilize the  $Id_i$  to find the corresponding point in  $\hat{\mathbf{Y}}_l$  and compute the point-wise difference vector between  $\hat{\mathbf{y}}_i$  and these points as

$$\mathbf{v}_{\hat{\mathbf{y}}_i} = \{g(\hat{\mathbf{y}}_i, \hat{\mathbf{y}}_j)\}_{j \in Id_i} \in \mathbb{R}^K. \quad (25)$$

Repeating the above step for all points in  $\hat{\mathbf{X}}_l$  and  $\hat{\mathbf{Y}}_l$ , we have  $V_{\hat{\mathbf{X}}_l} = [\mathbf{v}_{\hat{\mathbf{x}}_1}; \mathbf{v}_{\hat{\mathbf{x}}_2}; \dots; \mathbf{v}_{\hat{\mathbf{x}}_{N_l}}] \in \mathbb{R}^{N_l, K}$  and  $V_{\hat{\mathbf{Y}}_l} = [\mathbf{v}_{\hat{\mathbf{y}}_1}; \mathbf{v}_{\hat{\mathbf{y}}_2}; \dots; \mathbf{v}_{\hat{\mathbf{y}}_{N_l}}] \in \mathbb{R}^{N_l, K}$ . The two vectors reflect the local variation of two patches. Similar to some previous works [5], [31], we derive the variance and of  $\mathbf{V}_{\hat{\mathbf{X}}_l}$  and  $\mathbf{V}_{\hat{\mathbf{Y}}_l}$ , denoted by  $\sigma_{\hat{\mathbf{X}}_l}$  and  $\sigma_{\hat{\mathbf{Y}}_l}$ ; the co-variance between two vectors, denoted as  $c_{\hat{\mathbf{X}}_l, \hat{\mathbf{Y}}_l}$ . We finally compute one local feature related to the prediction term as

$$F_{2,l} = \frac{c_{\hat{\mathbf{X}}_l, \hat{\mathbf{Y}}_l} + T}{\sigma_{\hat{\mathbf{X}}_l} \cdot \sigma_{\hat{\mathbf{Y}}_l} + T}. \quad (26)$$

#### 4.5 Calculation of Visual Quality Score

For each local patch pair  $\mathbf{X}_l$  and  $\mathbf{Y}_l$ , we have two complexity based features  $F_{1,l}^O$  and  $F_{1,l}^I$  and one prediction based

feature  $F_{2,l}$ , which are both obtained via the SA-VAR. We then propose to fuse these features together to have two global indices for the entire distorted point cloud as

$$F_1 = \left( \frac{1}{L} \sum_l F_{1,l}^O \right) \cdot \left( \frac{1}{L} \sum_l F_{1,l}^I \right) \quad (27)$$

$$F_2 = \frac{1}{L} \sum_l F_{2,l}.$$

In the end, we can have the overall point cloud quality score by weighting the above global indices as

$$Q_l = \alpha F_1 + \beta F_2, \quad (28)$$

where  $\alpha$  and  $\beta$  are the weighting factors for two features.

## 5 EXPERIMENTAL EVALUATIONS

This section evaluates the proposed method and other state-of-the-art metrics for point cloud quality prediction, using five publicly accessible point cloud databases.

### 5.1 Databases and Evaluation Protocols

We review five PCQA databases used in our experiments as follows:

- SJTU-PCQA database [11]. There are 9 high-quality reference point cloud samples and 378 distorted samples provided with mean opinion scores (MOSSs). Each reference point cloud is augmented with 7 different types of impairments under 6 levels, including four individual distortions, Octree-based compression (OT), Color noise (CN), Geometry Gaussian noise (GGN), Downsampling (DS), and three superimposed distortions, i.e., Downsampling and Color noise (D+C), Downsampling and Geometry Gaussian noise (D+G), Color noise and Geometry Gaussian noise (C+G).

- WPC database [10]. There are 20 reference point clouds and 740 distorted point clouds generated from the references under five types of distortions, including Downsampling, Gaussian noise contamination, G-PCC(Trisoup), G-PCC(Octree), and V-PCC.

- M-PCCD database [54]. There are 8 reference point clouds and 232 distorted samples impaired by the MPED

TABLE 1  
PERFORMANCE COMPARISON OF DIFFERENT FR-PCQA METRICS ON FIVE DATABASES

Databases	SJTU-PCQA [11]			WPC [10]			M-PCCD [54]			ICIP2020 [55]			IRPC [56]			Weighted	
Criteria	PLCC	SROCC	RMSE	PLCC	SROCC	RMSE	PLCC	SROCC	RMSE	PLCC	SROCC	RMSE	PLCC	SROCC	PLCC	SROCC	
MSE-p2po [4]	0.877	0.791	1.166	0.578	0.566	18.708	0.778	0.797	0.855	0.888	0.878	0.522	0.769	0.714	0.625	0.710	0.683
MSE-p2pl [4]	0.753	0.676	1.596	0.488	0.446	20.013	0.815	0.836	0.788	0.913	0.915	0.463	0.749	0.682	0.647	0.641	0.602
Haussdorf-p2po [4]	0.742	0.681	1.628	0.398	0.258	21.028	0.593	0.366	1.095	0.601	0.542	0.908	0.401	0.044	0.895	0.528	0.391
Haussdorf-p2pl [4]	0.737	0.670	1.639	0.383	0.315	21.171	0.571	0.507	1.117	0.649	0.602	0.865	0.144	0.252	0.967	0.509	0.450
PSNR <sub>YUV</sub> [4]	0.652	0.644	1.841	0.551	0.536	19.132	0.654	0.66	1.029	0.868	0.867	0.564	0.721	0.673	0.677	0.618	0.608
PCQM [15]	0.860	0.847	1.237	0.751	0.743	15.132	0.900	0.915	0.594	0.969	0.970	0.280	0.897	0.831	0.433	0.820	0.813
GraphSIM [5]	0.856	0.841	1.071	0.694	0.680	16.498	0.932	0.945	0.493	0.890	0.872	0.518	0.850	0.716	0.514	0.790	0.775
MS-GraphSIM [16]	0.897	0.874	1.071	0.717	0.707	15.970	0.916	0.930	0.545	0.906	0.895	0.481	0.879	0.720	0.466	0.811	0.796
pointSSIM [57]	0.725	0.704	1.672	0.510	0.454	19.713	0.926	0.918	0.514	0.904	0.865	0.486	0.636	0.578	0.754	0.657	0.619
MPED [3]	0.896	0.884	1.076	0.700	0.678	16.374	0.824	0.849	0.770	0.964	0.952	0.303	0.923	0.842	0.376	0.793	0.779
TCMD	0.930	0.910	0.891	0.807	0.804	13.525	0.936	0.944	0.479	0.942	0.935	0.382	0.921	0.840	0.380	0.870	0.862

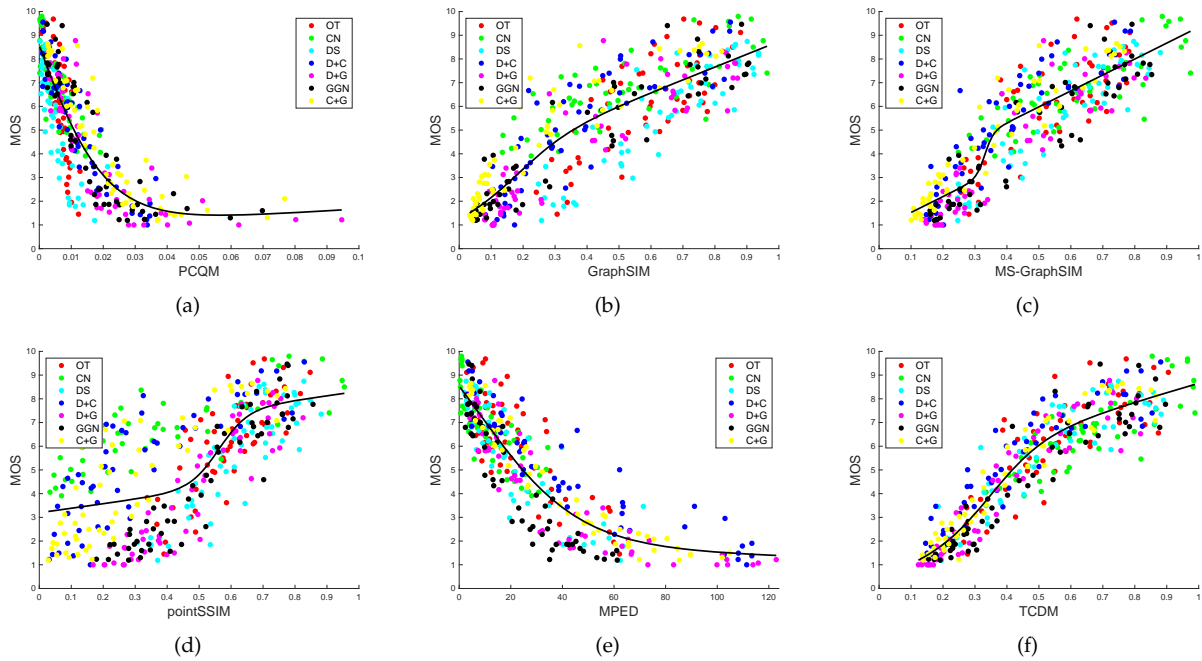


Fig. 6. Scatter plots of subject scores versus objective scores obtained by different model prediction for the SJTU-PCQA database. (a) PCQM; (b) GraphSIM; (c) MS-GraphSIM; (d) pointSSIM; (e) MPED; (f) TCDM.

encoders. The distortion results from the compression by V-PCC and four variations of G-PCC. The former is distributed into five levels, and the latter is split into six levels. Note that M-PCCD provides the MOS for both the reference and distorted samples. In our experiments we only use the MOSs of the distorted samples.

- ICIP2020 database [55]. There are 6 reference point clouds and 90 distorted point clouds and both references and distorted samples are provided with MOSs. The distortion results from the compression algorithms, including V-PCC, G-PCC(Trisoup) and G-PCC(Octree) under 5 levels. Similar to M-PCCD, we also only use the MOS of the distorted samples.

- IRPC database [56]. There are 6 reference point clouds and 54 distorted point clouds. Each native sample is distorted using three different compression methods (i.e., OT, G-PCC and V-PCC) with three compression levels (i.e., High quality - HQ, Medium quality - MQ, and Low quality - LQ). Note that IRPC provides three types of MOSs caused by

different rendering solutions. In our experiments, we use the MOSs resulting from "RColor" rendering. Please refer to [56] for more details.

To ensure the consistency between subjective scores (i.e., mean opinion scores) and objective predictions from various models, we first map the objective predictions of different models to the same dynamic range following the recommendations suggested by the video quality experts group (VQEG) [58]. Then, the Pearson linear correlation coefficient (PLCC), the Spearman rank order correlation coefficient (SROCC), and the root mean square error (RMSE) are utilized to evaluate the performance of different models, which indicate the linearity, monotonicity and accuracy, respectively. The larger PLCC or SROCC comes with better model performance. On the contrary, the lower RMSE is better. To map the dynamic range of the scores from objective quality assessment models into a common scale, the logistic regression recommended by VQEG is used. The formula is described below, according to the [58],



Fig. 7. Example point clouds corrupted by geometry Gaussian noise and color noise. The associated MOS values and objective scores of three metrics (GraphSIM, MPED, TCDM) are also provided. The values of 1-4 represent the rank of subjective values and objective scores in four distorted samples generated from one reference. For instance, 7.34(2) under the "GGN-level-1" sample of "Loot" represents that the sample has the MOS value of 7.34, which ranks 2nd out of four distorted samples of "Loot"

$$R_i = \beta_1 \left( \frac{1}{2} - \frac{1}{1 + \exp \beta_2 (Q_i - \beta_3)} \right) + \beta_4 Q_i + \beta_5 \quad (29)$$

where  $Q_i$  is the quality score of the  $i$ -th point cloud calculated by the PCQA model,  $R_i$  is the objective score after the regression, and  $\beta_1$ ,  $\beta_2$ ,  $\beta_3$ ,  $\beta_4$ , and  $\beta_5$  are the parameters fitted by minimizing the sum of squared errors between the regressive scores  $R_i$  and the subjective scores.

## 5.2 Parameter Setting

Several parameters are required to be determined in the proposed model:

*L in the space segmentation.* In the space segmentation, we need to determine the number of generating seeds  $L$  to create one 3D Voronoi diagram. We choose  $L = 400$  to balance the efficiency and complexity.

*K in the SA-VAR model.*  $K$  is used as the order of the SA-VAR model and as the number of neighbors in computing point-wise difference for prediction terms. Large  $K$  can effectively reduce the code length in the process of predictive coding while resulting in higher model complexity and computational cost.  $K = 20$  is finally set to achieve the trade-off between efficiency and complexity.

*T in the similarity pooling.* We simply set  $T = 0.000001$ .

*$\alpha, \beta$  in the feature fusion.*  $\alpha$  and  $\beta$  used in Eq. (27) determine the relative weight of two quality features. The SJTU-PCQA database is utilized as the training pool to choose

optimal weighted coefficients.  $\alpha = 0.3$  and  $\beta = 0.7$  are finally determined.

## 5.3 Overall Performance Comparison

Table 1 lists the experimental results on the five PCQA databases in terms of SROCC, PLCC, and RMSE. The proposed method, TCDM, is compared with several FR-PCQA metrics and we run all published codes to produce the results. Note that we use the PSNR measure for the first five point-based metrics and the L1 norm for MPED [3] and the color measure for pointSSIM [57].

For each database, the top two results for each evaluation criterion are highlighted in **boldface**. We can see that the proposed TCDM is among the top two performance in four databases except for ICIP 2020 and presents the best PLCC and RMSE on three databases including SJTU-PCQA, WPC and M-PCCD. Note that SJTU-PCQA, WPC and M-PCCD have more samples than ICIP2020 and IRPC, thus the evaluation results on the first three databases are more convincing than the last two. Moreover, to measure the average performance of these PCQA models across multiple databases, we also give the weighted mean (based on the size of these databases) values of PLCC and SROCC (weighted RMSE are not included since the ranges of RMSE values are not the same on the five databases) in the last column of Table 1. Our method outperforms the other state-of-art PCQA metrics with noticeable gains in terms of weighted criteria, having  $(\text{PLCC}, \text{SROCC}) = (0.870, 0.862)$ , followed by  $(0.820, 0.813)$  provided by PCQM and  $(0.811, 0.796)$  provided by MS-GraphSIM.

For better illustration, we also provide the scatter plots shown in Fig. 6 for multiple competing PCQA metrics (PCQM, GraphSIM, MS-GraphSIM, pointSSIM, MPED, TCDM) on the SJTU-PCQA databases. In all the plots, each point represents a test point cloud. The vertical axis denotes the subjective ratings of the perceived distortions and the horizontal axis denotes the metric score produced by objective metrics. The black curves in the scatter plots are obtained by the nonlinear fitting in Eq. 29. The algorithm's performance is considered superior when the scattered points are positioned in close proximity to the fitted curve. According to Fig. 6, it can be clearly seen from the figure that the objective scores predicted by TCDM correlate better with human judgments than other competitors because more points converge to the fitted curve, which further demonstrates the effectiveness of our method. Another interesting observation is that the scattered points of TCDM correlate better in low quality range than in high quality range. The reason may be that the TCDM is more capable of capturing these "visible distortion" while samples in the high quality range includes many invisible distortions due to the masking effect. One possible solution is to apply different strategies for high quality samples and low quality samples such as [59].

We further present some illustrative examples of distorted samples (from the SJTU-PCQA database) in Fig. 7, where corresponding distortion levels, MOS values, and objective scores of three metrics (GraphSIM, MPED, TCDM) are provided. We also annotate the rank of MOS values and three types of objective scores for four distorted samples

TABLE 2  
PERFORMANCE COMPARISON FOR FR-PCQA METRICS ON EACH INDIVIDUAL DISTORTION TYPE IN TERMS OF SROCC

SJTU-PCQA	M-p2po	M-p2pl	H-p2po	H-p2pl	PSNR <sub>YUV</sub>	PCQM	GraphSIM	MS-GraphSIM	PointSSIM	MPED	TCDM
OT	<b>0.825</b>	0.726	<b>0.849</b>	0.774	0.357	0.758	0.693	0.714	0.756	0.679	0.793
CN	-	-	-	-	0.753	<b>0.842</b>	0.778	0.770	0.797	<b>0.824</b>	0.819
DS	0.812	0.62	0.478	0.521	0.542	0.808	0.872	0.864	0.816	<b>0.878</b>	<b>0.876</b>
GGN	<b>0.950</b>	<b>0.950</b>	0.936	0.947	0.675	0.905	0.916	0.916	0.916	0.925	0.921
D+C	0.885	0.506	0.566	0.533	0.862	0.922	0.886	0.914	0.842	<b>0.937</b>	<b>0.934</b>
D+G	0.934	0.925	0.926	<b>0.946</b>	0.61	0.882	0.888	0.905	0.913	0.928	<b>0.944</b>
C+G	0.951	<b>0.959</b>	0.950	0.956	0.852	0.922	0.941	0.951	0.851	<b>0.969</b>	0.951
WPC	M-p2po	M-p2pl	H-p2po	H-p2pl	PSNR <sub>YUV</sub>	PCQM	GraphSIM	MS-GraphSIM	PointSSIM	MPED	TCDM
DS	<b>0.901</b>	<b>0.905</b>	0.849	0.857	0.707	0.875	0.898	0.887	0.836	0.897	0.882
C+G	0.729	0.689	0.738	0.692	0.777	<b>0.886</b>	0.840	0.869	0.587	<b>0.880</b>	0.857
G-PCC(O)	-	-	-	-	0.826	<b>0.894</b>	0.855	0.859	0.792	<b>0.869</b>	0.795
G-PCC(T)	0.465	0.293	0.463	0.353	0.646	0.821	0.816	<b>0.839</b>	0.681	0.551	<b>0.832</b>
V-PCC	<b>0.698</b>	0.445	<b>0.705</b>	0.566	0.345	0.643	0.612	0.631	0.366	0.476	0.640
M-PCCD	M-p2po	M-p2pl	H-p2po	H-p2pl	PSNR <sub>YUV</sub>	PCQM	GraphSIM	MS-GraphSIM	PointSSIM	MPED	TCDM
G-PCC(O)-lifting	0.900	0.867	0.899	0.878	0.722	0.932	0.963	<b>0.947</b>	0.940	0.904	<b>0.975</b>
G-PCC(O)-RAHT	0.884	0.842	0.879	0.851	0.735	0.923	<b>0.952</b>	0.939	0.940	0.901	<b>0.969</b>
G-PCC(T)-lifting	0.761	0.466	0.822	0.69	0.659	0.893	<b>0.938</b>	<b>0.917</b>	0.900	0.834	0.898
G-PCC(T)-RAHT	0.708	0.397	0.767	0.613	0.622	0.895	<b>0.927</b>	0.898	<b>0.958</b>	0.798	0.899
VPCC	0.277	0.149	0.550	0.125	0.317	0.736	<b>0.869</b>	0.824	<b>0.845</b>	0.531	0.814
ICIP2020	M-p2po	M-p2pl	H-p2po	H-p2pl	PSNR <sub>YUV</sub>	PCQM	GraphSIM	MS-GraphSIM	PointSSIM	MPED	TCDM
GPCC(O)	0.904	0.915	<b>0.942</b>	0.908	0.885	<b>0.968</b>	0.831	0.855	0.812	0.899	0.885
GPCC(T)	0.908	0.862	0.892	0.903	0.817	0.954	0.941	0.939	0.910	<b>0.955</b>	<b>0.970</b>
VPCC	0.723	0.295	0.828	0.708	0.848	<b>0.960</b>	0.720	0.770	0.822	<b>0.904</b>	0.822
IRPC	M-p2po	M-p2pl	H-p2po	H-p2pl	PSNR <sub>YUV</sub>	PCQM	GraphSIM	MS-GraphSIM	PointSSIM	MPED	TCDM
OT	0.818	0.892	0.895	0.902	0.538	0.868	0.858	0.849	0.912	<b>0.925</b>	<b>0.913</b>
GPCC(T)	0.656	0.629	0.525	0.898	0.831	0.901	0.792	0.809	0.588	<b>0.916</b>	<b>0.907</b>
VPCC	0.186	0.282	0.254	<b>0.435</b>	<b>0.686</b>	0.554	0.230	0.272	0.329	0.415	0.336

M-p2po	0	1	1	1	1	0	0	0	1	0	0
H-p2po	0	0	0	0	1	0	0	0	0	0	0
M-p2pl	0	0	0	0	1	0	0	0	0	0	0
H-p2pl	0	0	0	0	1	0	0	0	0	0	0
PSNR-YUV	0	0	0	0	0	0	0	0	0	0	0
PCQM	0	1	1	1	1	0	0	0	1	0	0
GraphSIM	0	1	1	1	1	0	0	0	1	0	0
MS-GraphSIM	1	1	1	1	1	0	1	0	0	0	0
pointSSIM	0	0	0	0	1	0	0	0	0	0	0
MPED	0	1	1	1	1	1	0	1	0	0	0
TCDM	1	1	1	1	1	1	1	1	1	1	0

(a)

M-p2po	0	1	1	1	0	0	0	0	0	0	0
H-p2po	0	0	0	0	0	0	0	0	0	0	0
M-p2pl	0	0	0	0	0	0	0	0	0	0	0
H-p2pl	0	0	0	0	0	0	0	0	0	0	0
PSNR-YUV	0	1	0	1	0	0	0	0	0	0	0
PCQM	1	1	1	1	1	0	1	1	0	1	0
GraphSIM	1	1	1	1	1	0	0	0	1	1	0
MS-GraphSIM	1	1	1	1	1	0	0	0	1	1	0
pointSSIM	0	1	0	1	0	0	0	0	0	0	0
MPED	0	1	0	1	0	0	0	0	0	0	0
TCDM	1	1	1	1	1	1	1	1	1	1	0

(b)

M-p2po	0	1	0	1	1	0	0	0	0	0	0
H-p2po	0	0	0	0	0	0	0	0	0	0	0
M-p2pl	0	1	0	1	1	0	0	0	0	0	0
H-p2pl	0	0	0	0	0	0	0	0	0	0	0
PSNR-YUV	0	0	0	0	0	0	0	0	0	0	0
PCQM	1	1	1	1	1	0	0	0	0	1	0
GraphSIM	1	1	1	1	1	0	0	0	1	1	0
MS-GraphSIM	1	1	1	1	1	0	0	0	0	1	0
pointSSIM	1	1	1	1	1	0	0	0	0	1	0
MPED	0	1	0	1	1	0	1	1	0	0	0
TCDM	1	1	1	1	1	1	1	1	1	0	1

(c)

M-p2po	0	1	0	1	0	0	0	0	0	0	0
H-p2po	0	0	0	0	0	0	0	0	0	0	0
M-p2pl	1	1	0	1	1	0	1	0	0	0	0
H-p2pl	0	0	0	0	0	0	0	0	0	0	0
PSNR-YUV	0	1	0	1	0	0	0	0	0	0	0
PCQM	1	1	1	1	1	0	1	1	0	1	0
GraphSIM	0	1	0	1	0	0	0	0	0	1	0
MS-GraphSIM	0	1	0	1	0	0	0	0	0	1	0
pointSSIM	0	1	0	1	0	0	0	0	0	0	0
MPED	1	1	1	1	1	0	1	1	1	0	1
TCDM	1	1	1	1	1	1	1	1	1	1	0

(d)

M-p2po	0	1	0	1	0	0	0	0	1	0	0
H-p2po	0	0	0	0	0	0	0	0	0	0	0
M-p2pl	0	1	0	1	0	0	0	0	1	0	0
H-p2pl	0	0	0	0	0	0	0	0	0	0	0
PSNR-YUV	0	1	0	1	0	0	0	0	0	0	0
PCQM	1	1	1	1	1	0	0	0	1	0	0
GraphSIM	0	1	0	1	1	0	0	0	1	0	0
MS-GraphSIM	0	1	1	1	1	0	0	0	1	0	0
pointSSIM	0	0	0	0	0	0	0	0	0	0	0
MPED	1	1	1	1	1	0	1	0	1	0	0
TCDM	1	1	1	1	1	1	0	1	0	1	0

(e)

Fig. 8. The results of statistical significance tests of the competing PCQA models on the (a) SJTU-PCQA; (b) WPC; (c) M-PCCD; (d) ICIP2020; (e) IRPC. A value of '1' (highlighted in navy blue) indicates that the model in the row is significantly better than the model in the column, while a value of '0' (highlighted in light blue) indicates that the first model is not significantly better than the second one.

TABLE 3  
PERFORMANCE COMPARISON FOR FR-PCQA METRICS ON SIAT-PCQD and WPC2.0 databases

SIAT-PCQD	M-p2po	M-p2pl	H-p2po	H-p2pl	PSNR <sub>YUV</sub>	PCQM	GraphSIM	MS-GraphSIM	PointSSIM	MPED	TCDM
PLCC	0.213	0.219	0.182	0.201	0.345	0.050	0.700	0.728	0.700	0.525	<b>0.736</b>
SROCC	0.17	0.185	0.179	0.185	0.339	0.618	0.613	0.628	0.631	0.473	<b>0.658</b>
RMSE	0.129	0.128	0.129	0.129	0.123	0.131	0.094	0.090	0.094	0.112	<b>0.089</b>
WPC2.0	M-p2po	M-p2pl	H-p2po	H-p2pl	PSNR <sub>YUV</sub>	PCQM	GraphSIM	MS-GraphSIM	PointSSIM	MPED	TCDM
PLCC	0.620	0.632	0.44	0.539	0.458	0.726	0.745	0.773	0.570	0.623	<b>0.803</b>
SROCC	0.583	0.594	0.350	0.400	0.452	0.726	0.751	0.777	0.568	0.628	<b>0.802</b>
RMSE	17.260	17.048	19.757	18.533	19.557	15.133	14.668	13.963	18.083	17.206	<b>13.100</b>

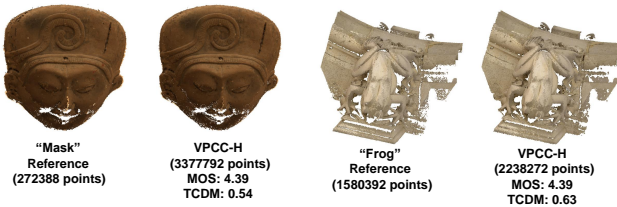


Fig. 9. Example point clouds corrupted by VPCC. The associated MOS values and TCDM scores are provided for each distorted samples. The point numbers of both reference and distorted samples are presented under each sample.

generated from one reference. For instance, "7.34(2)" under the "GGN-level-1" sample of "Loot" represents that the sample has the MOS value of 7.34, and it ranks 2nd out of four distorted samples of "Loot". Note that higher GraphSIM and TCDM values and lower MPED values indicate better quality. According to Fig. 7, we can see that: i) for each distortion type, as the point clouds are arranged in decreasing order of their MOS values, the objective scores of three metrics are in the same order as well, which states that all three metrics can accurately capture the rank among different levels of the same distortion; ii) GraphSIM and MPED both fail to reflect the correct rank between two distortion types. For example, the distorted sample of "Loot" under "CN-level-3" scheme has higher MOS than that under "GGN-level-3" scheme, but the objective scores provided by GraphSIM and MPED present reverse rank. The correct subjective rank for four distorted samples of "Loot" is "2,4,1,3", but the objective ranks of GraphSIM and MPED are "1,3,2,4" and "2,3,1,4", respectively. In comparison, the TCDM captures the difference between the two distortion types and presents lower scores for samples impaired by GGN, which contributes to the correct objective rank. According to the above example, we can conclude that the TCDM is more capable of differentiating the quality among various distortion types, leading to superior overall performance.

In order to draw statistically meaningful conclusions regarding the performance of the models, we conduct a series of hypothesis tests utilizing the prediction residuals obtained from each model's nonlinear regression. The findings of these significance tests are depicted in Fig. 8. Assuming that the prediction residuals of the models adhere to a Gaussian distribution, we employed the left-tailed F-test to compare the residuals of every pair of models

TABLE 4  
PERFORMANCE COMPARISON OF DIFFERENT COLOR SPACES ON SJTU-PCQA. .

Color Space	PLCC	SROCC	RMSE
RGB	0.9301	0.9102	0.8912
YUV	0.9294	0.9096	0.8957
GCM	0.9289	0.9099	0.8987

under examination. With a significance level of 0.05, a left-tailed F-test yielding a value of  $H = 1$  indicates that the first model (as denoted by the corresponding row in Fig. 8) exhibits superior performance to the second model (as denoted by the respective column in Fig. 8) with confidence exceeding 95%. Conversely, a value of  $H = 0$  suggests that the first model does not possess a statistically significant advantage over the second model. If the value  $H = 0$  holds consistently, regardless of which model is designated as the first one, it implies that the two models do not exhibit a significant disparity in performance. Fig. 8 (a)–(e) show the significant test results on the five databases, respectively. We see that TCDM performs the best on the SJTU-PCQA, WPC, and M-PCCD databases. On the ICIP2020 databases, TCDM is significantly better than all the other models except for PCQM and MPED. On the IRPC database, TCDM and MPED both perform very well and they have no statistically significant difference.

#### 5.4 Performance Comparison on Individual Distortion Type

Good (bad) overall performance does not necessarily mean good (bad) performance for individual distortion types. Therefore, we compare the performance of FR-PCQA metrics towards different point cloud distortions on the five databases. SROCC scores are shown as the only evaluation measure and the results are shown in Table 2. For each distortion type in each database, we also use **boldface** to highlight the algorithm with the top two SROCC among all competing metrics.

There exist 23 distortion types on the five databases. According to Table 2, MPED is among the top 2 models 10 times, followed by 9 times for the proposed TCDM and 6 times for PCQM. In general, our method is more capable of coping with the distortions caused by downsampling and G-PCC compression. We notice that TCDM provides lower SROCC than PCQM and MPED over VPCC on the ICIP2020 and IRPC databases, which leads to its relatively inferior performance on these databases. Another noticeable phenomenon is that the TCDM shows inconsistent

TABLE 5  
PERFORMANCE COMPARISON OF DIFFERENT SAMPLING STRATEGIES ON SJTU-PCQA

Strategy	$L$	PLCC	SROCC	RMSE
RS	100	0.9282	0.9079	0.903
	200	<b>0.9313</b>	<b>0.9118</b>	<b>0.8841</b>
	400	0.9293	0.9102	0.8961
	1000	0.9270	0.9099	0.9102
FPS	100	0.9291	0.9075	0.8976
	200	<b>0.9306</b>	0.9099	<b>0.8881</b>
	400	0.9301	<b>0.9102</b>	0.8912
	1000	0.9260	0.9080	0.9161

prediction performances across the different databases for V-PCC. Specifically, for V-PCC, TCDM performs relatively well on M-PCCD while providing bad results on IRPC. Further looking into this issue, we find that the extent of point number augmentation caused by VPCC relies on the sparsity of the original point cloud, which further influences the performance of TCDM on VPCC. To better illustrate it, we show several visual samples (provided in IRPC database) in Fig. 9 to show the impact of point number augmentation on TCDM. Given two reference point clouds "Mask" 272388 points and "Frog" with 1580392 points, their VPCC compressed samples at a high level ((denoted as "VPCC-H") share the same MOS scores of 4.39. However, due to the sparsity of the "Mask" reference, the impact of the increased point number after VPCC is far greater than that of the "Frog" reference. Specifically, VPCC compressed "Mask" at the high level increases the point number by 1140% (from 272388 to 3377792) while VPCC compressed "Frog" at the high level only increases the point number by 42% (from 1580392 to 2238272). Note that the TCDM finds  $k$  nearest neighbors for each point of the reference point cloud in the reference and distorted point clouds. Therefore, the significant point number augmentation of "Mask" inevitably impacts the kNN search process of TCDM, thus influencing the prediction of objective scores. Specifically, although distorted samples of "Mask" and "Frog" under the "VPCC-H" scheme share the same MOS values of 4.39, TCDM exhibits a lower objective score for the compressed sample of "Mask", thereby impairing the performance of TCDM on VPCC.

It is worth pointing out that the substantial increase in the point number observed in the "Mask" sample is not common. VPCC is designed for compressing dense point clouds such as the "Frog" sample, and the significant increase in the point number of the "Mask" sample is mainly due to its sparsity. We further test TCDM and competing metrics on two PCQA databases that only consist of VPCC distorted samples, i.e., SIAT-PCQD database (340 samples) [60] and WPC2.0 database (400 samples) [61]. Note that the reference point clouds used in SIAT-PCQD database and WPC2.0 database are all dense. We show the performance of different metrics on SIAT-PCQD and WPC2.0 databases in Tab 3. According to Tab 3, we can see that the TCDM outperforms other competing metrics in terms of three criteria, which demonstrate the effectiveness of TCDM for most cases of VPCC.

TABLE 6  
PERFORMANCE COMPARISON (IN TERMS OF SROCC) OF DIFFERENT SPATIAL WEIGHTS

	Databases	SJTU	WPC	M-PCCD	ICIP2020	IRPC	Weighted
$d_{i,j}$	1	<b>0.9143</b>	0.8021	<b>0.9478</b>	0.9300	0.8051	0.8609
	$1/\ \mathbf{x}_i - \mathbf{x}_j\ _2$	0.8937	0.7975	0.9349	<b>0.9367</b>	0.7934	0.8514
	$\exp(-\ \mathbf{x}_i - \mathbf{x}_j\ _2/\eta)$	0.9056	0.7982	0.9354	0.9322	0.8198	0.8557
	Proposed	0.9102	<b>0.8041</b>	0.9437	0.9354	<b>0.8401</b>	<b>0.8618</b>

TABLE 7  
PERFORMANCE COMPARISON (IN TERMS OF SROCC) OF DIFFERENT NEIGHBORHOOD SCALES

	Databases	SJTU-PCQA	WPC	M-PCCD	ICIP2020	IRPC	Weighted
K	10	0.9009	0.7757	0.9379	0.9307	0.8293	0.8438
	20	0.9102	<b>0.8041</b>	0.9437	<b>0.9354</b>	0.8401	<b>0.8618</b>
	30	0.9154	0.7806	0.9454	0.9295	0.8485	0.8517
	50	<b>0.9159</b>	0.7695	<b>0.9456</b>	0.9275	<b>0.8543</b>	0.8465

## 5.5 Impact of Key Modules and Parameter Values

### 5.5.1 Color Space

We have exemplified the effectiveness of TCDM based on the RGB-based color channel decomposition. In this part, we test the performance of TCDM in terms of other color channel spaces, e.g., YUV and Gaussian color model (GCM) [62]. YUV and GCM are two color channel spaces that consist of one luminance component and two chrominance components. Given that the human visual system is more sensitive to the luminance component, we set  $k_l = 6$ ,  $k_{c1} = k_{c2} = 1$  [5] when calculating the point-wise difference vector in Eq. (24).  $k_l$  represents the weighting factors of the luminance component, and  $k_{c1}$ ,  $k_{c2}$  for chrominance components. We use SJTU-PCQA as the test database and the results are shown in Table 4. In Table 4, we see that the performance of TCDM is very close for multiple color spaces, which validates the robustness of TCDM.

### 5.5.2 Sampling Strategy

In Section 4.2, we leverage farthest point sampling (FPS) to obtain the generating seeds of the 3D Voronoi diagram. We further test the model performance with random sampling (RS) at various sampling ratios  $L$ . As shown in Table 5, we can see that both RS and FPS retain consistent correlation with MOSs across different  $L$ .  $L = 400$  presents the best SROCC under FPS while  $L = 200$  outperforms other sampling ratios under RS. Too large or too small  $L$  weakens the performance slightly. Although FPS can attain more uniform sampling than RS, the 3D Voronoi diagram achieves non-overlapping and non-omission divisions for both two strategies. It states that our model can keep reliable performance under different sampling strategies and sampling ratios.

### 5.5.3 Spatial Weight

The spatial weight is employed to strengthen the AR's capability of capturing irregular spatial structure. We further test the model performance (in terms of SROCC) with different  $d_{i,j}$  in Eq. (11) and show the result in Table 6. We can see that not all distance-related spatial weights provide better performance than constant weight. For instance,  $d_{i,j} = 1/\|\mathbf{x}_i - \mathbf{x}_j\|_2$  shows poorer correlation than  $d_{i,j} = 1$ , which may be caused by its large range of  $(0, +\infty)$  and steep function curve at small distances. In comparison, the

TABLE 8  
PERFORMANCE COMPARISON (IN TERMS OF SROCC) FOR  
FEATURE COMBINATION

Databases	SJTU-PCQA	WPC	M-PCCD	ICIP2020	IRPC	Weighted
$F_1$	0.7913	0.5110	0.8411	0.8693	0.5217	0.6552
$F_2$	0.8721	0.7863	0.8800	0.9181	0.7294	0.8324
TCDM	<b>0.9102</b>	<b>0.8041</b>	<b>0.9437</b>	<b>0.9354</b>	<b>0.8401</b>	<b>0.8618</b>

proposed  $d_{i,j}$  is in the range of  $[0.5,1]$ , which avoids overestimating or underestimating some points too much. In general, the proposed spatial weight presents better SROCC than  $d_{i,j} = 1$  on three databases (i.e., WPC, ICIP2020, and IRPC) and weighted criteria. In particular, the proposed weight yields a noticeable gain on IRPC than  $d_{i,j} = 1$ , which states that introducing proper spatial weight in the AR model is beneficial for PCQA.

#### 5.5.4 Neighborhood Scale

$K$  is used as the order of the SA-VAR model and as the number of neighbors in computing point-wise difference for prediction terms. We test the performance of TCDM under different  $K$  to investigate the influence of scales and show the results in TABLE 7. We see that  $K = 20$  provides the best performance on WPC and ICIP2020 while  $K = 50$  stands out on the other three databases. It is worth noting that larger  $K$  lead to higher computational costs. Therefore we choose  $K = 20$  in our model to achieve a better trade-off between effectiveness and complexity.

#### 5.5.5 Feature Combination

There are two features involved in our model, i.e., the complexity-based feature  $F_1$  and the prediction-based feature  $F_2$ . To investigate the contribution of these two components, we respectively test them on the five databases and illustrate the results in Table 8. We see that: i) the prediction-based feature  $F_2$  outperforms the complexity-based feature  $F_1$  on the five databases; ii) the proposed TCDM combining both  $F_1$  and  $F_2$  shows better performance than using  $F_1$  or  $F_2$  alone, which demonstrates the complementarity of the two components.

## 6 CONCLUSION

In this paper, we propose a novel full-reference point cloud quality metric from the perspective of transformational complexity. Supposing that the point cloud quality can be described as the complexity of transforming the distorted point cloud back to its reference, we utilize one space-aware vector autoregressive model to encode multiple channels of the reference point cloud in cases with and without its distorted version. Two complexity terms are pooled into one complexity-based feature and the prediction terms generated by SA-VAR are further introduced to achieve more robust quality prediction. The proposed metric, denoted as TCDM, shows a consistent and reliable correlation with the subjective MOSs on five point cloud quality assessment databases, presenting noticeable gains over the state-of-the-art FR-PCQA metrics. Further experiments have supported model generalization by examining its key modules and parameter values.

## REFERENCES

- [1] Z. Shan, Q. Yang, R. Ye, Y. Zhang, Y. Xu, X. Xu, and S. Liu, "Gpant: No-reference point cloud quality assessment with multi-task graph convolutional network," *IEEE Transactions on Visualization and Computer Graphics*, 2022.
- [2] Q. Liu, H. Su, T. Chen, H. Yuan, and R. Hamzaoui, "No-reference bitstream-layer model for perceptual quality assessment of v-pcc encoded point clouds," *IEEE Transactions on Multimedia*, 2022.
- [3] Q. Yang, Y. Zhang, S. Chen, Y. Xu, J. Sun, and Z. Ma, "Mped: Quantifying point cloud distortion based on multiscale potential energy discrepancy," *IEEE Transactions on Pattern Analysis and Machine Intelligence*, pp. 1–18, 2022.
- [4] Mpeg reference software. [Online]. Available: <http://mpegx.int-evry.fr/software/MPEG/PCC/TM/mpeg-pcc-dmetric>
- [5] Q. Yang, Z. Ma, Y. Xu, Z. Li, and J. Sun, "Inferring point cloud quality via graph similarity," *IEEE Transactions on Pattern Analysis and Machine Intelligence*, 2020.
- [6] G. Lavoué, M. C. Larabi, and L. Vánsa, "On the efficiency of image metrics for evaluating the visual quality of 3d models," *IEEE Transactions on Visualization and Computer Graphics*, vol. 22, no. 8, pp. 1987–1999, 2015.
- [7] R. L. De Queiroz and P. A. Chou, "Motion-compensated compression of dynamic voxelized point clouds," *IEEE Transactions on Image Processing*, vol. 26, no. 8, pp. 3886–3895, 2017.
- [8] E. Alexiou and T. Ebrahimi, "Exploiting user interactivity in quality assessment of point cloud imaging," in *2019 Eleventh International Conference on Quality of Multimedia Experience (QoMEX)*, 2019, pp. 1–6.
- [9] A. Javaheri, C. Brites, F. Pereira, and J. Ascenso, "Joint geometry and color projection-based point cloud quality metric," *IEEE Access*, 2022.
- [10] Q. Liu, H. Su, Z. Duanmu, W. Liu, and Z. Wang, "Perceptual quality assessment of colored 3d point clouds," *IEEE Transactions on Visualization and Computer Graphics*, 2022.
- [11] Q. Yang, H. Chen, Z. Ma, Y. Xu, R. Tang, and J. Sun, "Predicting the perceptual quality of point cloud: A 3d-to-2d projection-based exploration," *IEEE Transactions on Multimedia*, vol. 23, pp. 3877–3891, 2020.
- [12] Z. He, G. Jiang, Z. Jiang, and M. Yu, "Towards a colored point cloud quality assessment method using colored texture and curvature projection," in *2021 IEEE International Conference on Image Processing (ICIP)*. IEEE, 2021, pp. 1444–1448.
- [13] Q. Yang, Y. Liu, S. Chen, Y. Xu, and J. Sun, "No-reference point cloud quality assessment via domain adaptation," in *Proceedings of the IEEE/CVF Conference on Computer Vision and Pattern Recognition (CVPR)*, June 2022, pp. 21 179–21 188.
- [14] G. Meynet, J. Digne, and G. Lavoué, "Pc-msdm: A quality metric for 3d point clouds," in *2019 Eleventh International Conference on Quality of Multimedia Experience (QoMEX)*. IEEE, 2019, pp. 1–3.
- [15] G. Meynet, Y. Nehmé, J. Digne, and G. Lavoué, "Pcq: A full-reference quality metric for colored 3d point clouds," in *2020 Twelfth International Conference on Quality of Multimedia Experience (QoMEX)*, 2020, pp. 1–6.
- [16] Y. Zhang, Q. Yang, and Y. Xu, "Ms-graphsim: Inferring point cloud quality via multiscale graph similarity," in *Proceedings of the 29th ACM International Conference on Multimedia*, 2021, pp. 1230–1238.
- [17] R. Diniz, P. G. Freitas, and M. C. Farias, "Local luminance patterns for point cloud quality assessment," in *2020 IEEE 22nd International Workshop on Multimedia Signal Processing (MMSP)*. IEEE, 2020, pp. 1–6.
- [18] R. Diniz, P. G. Freitas, and M. C. Q. Farias, "Towards a point cloud quality assessment model using local binary patterns," in *2020 Twelfth International Conference on Quality of Multimedia Experience (QoMEX)*, 2020, pp. 1–6.
- [19] E. Alexiou, I. Viola, and P. Cesar, "Pointpca: Point cloud objective quality assessment using pca-based descriptors," *arXiv preprint arXiv:2111.12663*, 2021.
- [20] G. Lavoué, "A multiscale metric for 3d mesh visual quality assessment," in *Computer graphics forum*, vol. 30, no. 5. Wiley Online Library, 2011, pp. 1427–1437.
- [21] Y. Nehmé, F. Dupont, J.-P. Farrugia, P. Le Callet, and G. Lavoué, "Visual quality of 3d meshes with diffuse colors in virtual reality: Subjective and objective evaluation," *IEEE Transactions on Visualization and Computer Graphics*, vol. 27, no. 3, pp. 2202–2219, 2020.
- [22] U. Hahn, N. Chater, and L. B. Richardson, "Similarity as transformation," *Cognition*, vol. 87, no. 1, pp. 1–32, 2003.

- [23] R. L. Goldstone and J. Y. Son, *Similarity*. Oxford University Press, 2012.
- [24] T. Guha and R. K. Ward, "Image similarity using sparse representation and compression distance," *IEEE Transactions on Multimedia*, vol. 16, no. 4, pp. 980–987, 2014.
- [25] Y. Lan and R. Harvey, "Image classification using compression distance," in *VVG*, 2005, pp. 173–180.
- [26] M. Li, P. Vitányi *et al.*, *An introduction to Kolmogorov complexity and its applications*. Springer, 2008, vol. 3.
- [27] P. M. Vitányi, "How incomputable is kolmogorov complexity?" *Entropy*, vol. 22, no. 4, p. 408, 2020.
- [28] M. Li, X. Chen, X. Li, B. Ma, and P. M. Vitányi, "The similarity metric," *IEEE transactions on Information Theory*, vol. 50, no. 12, pp. 3250–3264, 2004.
- [29] M. W. Spratling, "A review of predictive coding algorithms," *Brain and cognition*, vol. 112, pp. 92–97, 2017.
- [30] K. Friston and S. Kiebel, "Predictive coding under the free-energy principle," *Philosophical transactions of the Royal Society B: Biological sciences*, vol. 364, no. 1521, pp. 1211–1221, 2009.
- [31] Z. Wang, A. C. Bovik, H. R. Sheikh, and E. P. Simoncelli, "Image quality assessment: from error visibility to structural similarity," *IEEE transactions on image processing*, vol. 13, no. 4, pp. 600–612, 2004.
- [32] H. R. Sheikh and A. C. Bovik, "Image information and visual quality," *IEEE Transactions on image processing*, vol. 15, no. 2, pp. 430–444, 2006.
- [33] Z. Wang and Q. Li, "Information content weighting for perceptual image quality assessment," *IEEE Transactions on image processing*, vol. 20, no. 5, pp. 1185–1198, 2010.
- [34] E. Alexiou and T. Ebrahimi, "Point cloud quality assessment metric based on angular similarity," in *2018 IEEE International Conference on Multimedia and Expo (ICME)*. IEEE, 2018, pp. 1–6.
- [35] A. Javaheri, C. Brites, F. Pereira, and J. Ascenso, "A generalized hausdorff distance based quality metric for point cloud geometry," in *2020 Twelfth International Conference on Quality of Multimedia Experience (QoMEX)*. IEEE, 2020, pp. 1–6.
- [36] C. H. Bennett, P. Gács, M. Li, P. M. Vitányi, and W. H. Zurek, "Information distance," *IEEE Transactions on information theory*, vol. 44, no. 4, pp. 1407–1423, 1998.
- [37] R. Cilibrasi and P. M. Vitányi, "Clustering by compression," *IEEE Transactions on Information theory*, vol. 51, no. 4, pp. 1523–1545, 2005.
- [38] N. Nikvand and Z. Wang, "Image distortion analysis based on normalized perceptual information distance," *Signal, Image and Video Processing*, vol. 7, no. 3, pp. 403–410, 2013.
- [39] Y. Huang and R. P. Rao, "Predictive coding," *Wiley Interdisciplinary Reviews: Cognitive Science*, vol. 2, no. 5, pp. 580–593, 2011.
- [40] D. O'Shaughnessy, "Linear predictive coding," *IEEE potentials*, vol. 7, no. 1, pp. 29–32, 1988.
- [41] F. Itakura, "Minimum prediction residual principle applied to speech recognition," *IEEE Transactions on Acoustics, Speech, and Signal Processing*, vol. 23, no. 1, pp. 67–72, 1975.
- [42] P. Wang, R. Dai, and I. F. Akyildiz, "A spatial correlation-based image compression framework for wireless multimedia sensor networks," *IEEE Transactions on Multimedia*, vol. 13, no. 2, pp. 388–401, 2010.
- [43] S. Schwarz, M. Preda, V. Baroncini, M. Budagavi, P. Cesar, P. A. Chou, R. A. Cohen, M. Krivokuća, S. Lasserre, Z. Li *et al.*, "Emerging mpeg standards for point cloud compression," *IEEE Journal on Emerging and Selected Topics in Circuits and Systems*, vol. 9, no. 1, pp. 133–148, 2018.
- [44] S. Lee, M. S. Pattichis, and A. C. Bovik, "Foveated video quality assessment," *IEEE Transactions on Multimedia*, vol. 4, no. 1, pp. 129–132, 2002.
- [45] L. Hua, M. Yu, Z. He, R. Tu, and G. Jiang, "Cpc-gsct: Visual quality assessment for coloured point cloud based on geometric segmentation and colour transformation," *IET Image Processing*, vol. 16, no. 4, pp. 1083–1095, 2022.
- [46] Y. Eldar, M. Lindenbaum, M. Porat, and Y. Y. Zeevi, "The farthest point strategy for progressive image sampling," *IEEE Transactions on Image Processing*, vol. 6, no. 9, pp. 1305–1315, 1997.
- [47] G. Zhai, X. Wu, X. Yang, W. Lin, and W. Zhang, "A psychovisual quality metric in free-energy principle," *IEEE Transactions on Image Processing*, vol. 21, no. 1, pp. 41–52, 2011.
- [48] J. Wu, W. Lin, G. Shi, and A. Liu, "Perceptual quality metric with internal generative mechanism," *IEEE Transactions on Image Processing*, vol. 22, no. 1, pp. 43–54, 2012.
- [49] X. Zhang and X. Wu, "Image interpolation by adaptive 2-d autoregressive modeling and soft-decision estimation," *IEEE transactions on image processing*, vol. 17, no. 6, pp. 887–896, 2008.
- [50] X. Wu, G. Zhai, X. Yang, and W. Zhang, "Adaptive sequential prediction of multidimensional signals with applications to lossless image coding," *IEEE Transactions on Image Processing*, vol. 20, no. 1, pp. 36–42, 2010.
- [51] K. Gu, J. Qiao, X. Min, G. Yue, W. Lin, and D. Thalmann, "Evaluating quality of screen content images via structural variation analysis," *IEEE Transactions on Visualization and Computer Graphics*, vol. 24, no. 10, pp. 2689–2701, 2017.
- [52] M. A. Irfan and E. Magli, "Joint geometry and color point cloud denoising based on graph wavelets," *IEEE Access*, vol. 9, pp. 21 149–21 166, 2021.
- [53] K. Takeuchi, H. Kashima, and N. Ueda, "Autoregressive tensor factorization for spatio-temporal predictions," in *2017 IEEE International Conference on Data Mining (ICDM)*. IEEE, 2017, pp. 1105–1110.
- [54] E. Alexiou, I. Viola, T. M. Borges, T. A. Fonseca, R. L. De Queiroz, and T. Ebrahimi, "A comprehensive study of the rate-distortion performance in mpeg point cloud compression," *APSIPA Transactions on Signal and Information Processing*, vol. 8, 2019.
- [55] S. Perry, H. P. Cong, L. A. da Silva Cruz, J. Prazeres, M. Pereira, A. Pinheiro, E. Dumic, E. Alexiou, and T. Ebrahimi, "Quality evaluation of static point clouds encoded using mpeg codecs," in *2020 IEEE International Conference on Image Processing (ICIP)*. IEEE, 2020, pp. 3428–3432.
- [56] A. Javaheri, C. Brites, F. Pereira, and J. Ascenso, "Point cloud rendering after coding: Impacts on subjective and objective quality," *IEEE Transactions on Multimedia*, vol. 23, pp. 4049–4064, 2020.
- [57] E. Alexiou and T. Ebrahimi, "Towards a point cloud structural similarity metric," in *2020 IEEE International Conference on Multimedia & Expo Workshops (ICMEW)*. IEEE, 2020, pp. 1–6.
- [58] VQEG, "Final report from the video quality experts group on the validation of objective models of video quality assessment," [online]. Available: <http://www.its.blrdoc.gov/vqeg/vqeg-home.aspx>.
- [59] E. C. Larson and D. M. Chandler, "Most apparent distortion: full-reference image quality assessment and the role of strategy," *Journal of electronic imaging*, vol. 19, no. 1, pp. 011 006–011 006, 2010.
- [60] X. Wu, Y. Zhang, C. Fan, J. Hou, and S. Kwong, "Subjective quality database and objective study of compressed point clouds with 6dof head-mounted display," *IEEE Transactions on Circuits and Systems for Video Technology*, vol. 31, no. 12, pp. 4630–4644, 2021.
- [61] Q. Liu, H. Yuan, R. Hamzaoui, H. Su, J. Hou, and H. Yang, "Reduced reference perceptual quality model with application to rate control for video-based point cloud compression," *IEEE Trans. Image Processing*, vol. 30, pp. 6623–6636, 2021.
- [62] J.-M. Geusebroek, R. Van Den Boomgaard, A. W. Smeulders, and A. Dev, "Color and scale: The spatial structure of color images," in *European Conf. Computer Vision (ECCV'00)*. Springer, 2000, pp. 331–341.